Remote Sensing of Environment 311 (2024) 114294

Contents lists available at ScienceDirect

Remote Sensing of Environment

journal homepage: www.elsevier.com/locate/rse

Comparing the quantum use efficiency of red and far-red sun-induced fluorescence at leaf and canopy under heat-drought stress

Sebastian Wieneke [a,b,c,*], Javier Pacheco-Labrador [d,e], Miguel D. Mahecha [a,b,f], Sílvia Poblador [c,g], Sara Vicca [h], Ivan A. Janssens [c]

[a] Institute for Earth System Science and Remote Sensing, Leipzig University, Leipzig, Germany
[b] German Centre for Integrative Biodiversity Research (iDiv) Halle–Jena–Leipzig, Leipzig, Germany
[c] Plants and Ecosystems (PLECO), Department of Biology, University of Antwerp, Wilrijk, Belgium
[d] Environmental Remote Sensing and Spectroscopy Laboratory (SpecLab), Spanish National Research Council, Albasanz 26-28, 28037, Madrid, Spain
[e] Max Planck Institute for Biogeochemistry (MPI-BGC), Hans Knöll Straße 10, Jena D-07745, Germany
[f] Helmholtz Centre for Environmental Research (UFZ), Leipzig, Germany
[g] Departament de Biologia Evolutiva, Ecologia i Ciències Ambientals (BEECA), Universitat de Barcelona, Av. Diagonal 643, 08028 Barcelona, Spain
[h] Biobased Sustainability Engineering (SUSTAIN), Department of Bioscience Engineering, University of Antwerp, Groenenborgerlaan 171, 2020 Antwerpen, Belgium

ARTICLE INFO

Editor: Jing M. Chen

Keywords:
Sun induced fluorescence
Red fluorescence
Far-red fluorescence
Reabsorption correction
Drought and heat stress

ABSTRACT

Sun-Induced chlorophyll Fluorescence (SIF) is the most promising remote sensing signal to monitor photosynthesis in space and time. However, under stress conditions its interpretation is often complicated by factors such as light absorption and plant morphological and physiological adaptations. To ultimately derive the quantum yield of fluorescence (Φ_F) at the photosystem from canopy measurements, the so-called escape probability (f_{esc}) needs to be accounted for.

In this study, we aim to compare Φ_F measured at leaf- and canopy-scale to evaluate the influence of stress responses on the two signals based on a potato mesocosm heat-drought experiment. First, we compared the performance of recently proposed reflectance-based approaches to estimate leaf and canopy red f_{esc} using data-supported simulations of the radiative transfer model SCOPE. While the leaf red f_{esc} showed a strong correlation ($r^2 \geq 0.76$), the canopy red f_{esc} exhibited no relationship with the SCOPE retrieved red f_{esc} in our experiment. We therefore propose modifications to the canopy model to address this limitation.

We then used the modified models of red f_{esc}, along with an existing model for far-red f_{esc} to analyse the dynamics of leaf and canopy red and far-red fluorescence under increasing drought and heat stress conditions. By incorporating f_{esc}, we obtained a closer agreement between leaf and canopy measurements. Specifically, for red f_{esc}, the r^2 of the two variables increased from 0.3 to 0.50, and for far-red f_{esc}, from 0.36 to 0.48.

When comparing the dynamics of the quantum yield of red and far-red fluorescence ($\Phi_{F,687}$ and $\Phi_{F,760}$) under increasing stress, we observed a statistically significant decrease of both leaf and canopy $\Phi_{F,687}$ as well as leaf $\Phi_{F,760}$, as drought and heat conditions intensified. Canopy $\Phi_{F,760}$, on the contrary, did not exhibit the same trend, since measurements under low stress conditions showed a wider spread and lower median than under high stress conditions. Finally, we analysed the sensitivity of $\Phi_{F,687}$ and $\Phi_{F,760}$ to changing solar incidence angle, by comparing the variability of the measurements without and with mesocosm rotation. Our results suggest that the variation in $\Phi_{F,760}$ strongly increased with changing solar incidence angle. These findings highlight the need for further research to understand the causes of discrepancies between leaf and canopy scale $\Phi_{F,760}$. On the contrary, the underutilised and understudied $\Phi_{F,687}$ showed great potential in assessing plant responses to drought and heat stress.

* Corresponding author at: Remote Sensing Centre for Earth System Research (RSC4Earth), Faculty of Physics and Earth Sciences, University of Leipzig, Leipzig, Germany.
E-mail address: sebastian.wieneke@uni-leipzig.de (S. Wieneke).

https://doi.org/10.1016/j.rse.2024.114294
Received 11 June 2023; Received in revised form 8 June 2024; Accepted 22 June 2024
Available online 26 June 2024

1. Introduction

Vegetation indices (VIs) derived from various remote sensing platforms (Montero et al., 2023) are widely used to predict photosynthesis in space and time. However, except for the photochemical reflectance index (PRI; Gamon et al., 1997), classical greenness-based VIs do not capture physiological modulation of photosynthesis. Sun-Induced Fluorescence (SIF) on the other hand, is directly linked to the photosynthetic light reactions and is therefore often referenced as the most promising estimator of photosynthesis (Mohammed et al., 2019; Porcar-Castell et al., 2021).

After being absorbed by chlorophyll, light energy can mainly follow four pathways: i) drive the photochemical reactions (photochemical quenching; PQ), ii) the release as heat (non-photochemical quenching; NPQ), iii) reemission as chlorophyll *a* fluorescence (ChlaF) and iv) the nonradiative transfer of excitation energy (Lichtenthaler and Rinderle, 1988; Porcar-Castell et al., 2021; Porcar-Castell et al., 2014; Van Wittenberghe et al., 2021). Non-photochemical quenching (NPQ) is a protective mechanism used by plants to dissipate excess absorbed light energy as heat, thereby preventing the formation of harmful reactive oxygen species and protecting the photosynthetic machinery from damage. An increase in the quantum efficiency of NPQ (Φ_{NPQ}) leads to a reduction in PQ and, consequently, in the quantum efficiency of photochemistry (Φ_P) (Butler, 1978; Müller et al., 2001). ChlaF (mW $m^{-2}sr^{-1}nm^{-1}$) is the light that is emitted within photosystem II and I (PSII & PSI) when chlorophyll excited electrons return to their ground state. ChlaF is emitted between 650 and 800 nm and shows two distinct peaks at 680 (F_{red}) and 740 nm ($F_{far\text{-}red}$), with F_{red} being mainly related to fluorescence emission of Photosystem II (PSII), and $F_{far\text{-}red}$ comprising fluorescence emission from both PSII and PSI (Buschmann, 2007). Given the unique contributions of each photosystem to the fluorescence spectrum, the relationship between F_{red} and $F_{far\text{-}red}$ is expected to vary under different stress conditions (Ač et al., 2015; Mohammed et al., 2019). In their meta-analysis, Ač et al. (2015) demonstrated, for instance, that canopy F_{red} and $F_{far\text{-}red}$ decrease under water stress, while their ratio increase in response to nitrogen deficit. As the down-regulation of photosynthesis by NPQ is primarily associated with PSII (Müller et al., 2001), F_{red} is expected to have a stronger association with NPQ and PQ than $F_{far\text{-}red}$. Despite the closer association between F_{red} and NPQ/PQ, most publications related to SIF focus on the far-red peak for three reasons. Firstly, retrievals from satellite platforms typically focus on far-red SIF, with only limited retrievals available for red SIF (Joiner et al., 2016; Köhler et al., 2020; Zhao et al., 2022). Secondly, due to the deeper oxygen absorption bands, the retrieval of far-red SIF is associated with a higher signal-to-noise ratio (SNR) and shows thus lower uncertainty compared to red SIF (Cendrero-Mateo et al., 2019; Cogliati et al., 2015; Damm et al., 2011). Lastly, red SIF is reabsorbed by chlorophyll within the leaf and through the canopy, (Rossini et al., 2015; Van Wittenberghe et al., 2013), which complicates the interpretation in particular under drought stress conditions (Magney et al., 2019).

SIF can be expressed as the product of the absorbed photosynthetically active radiation (*APAR*), the quantum yield of fluorescence (Φ_F) and the escape probability (f_{esc}). Where f_{esc} refers to the probability that the photons emitted by chlorophyll fluorescence will escape the canopy, in the direction of the sensor, without being absorbed or scattered by other plant materials (Guanter et al., 2014).

$$SIF = APAR \bullet \Phi_F \bullet f_{esc} \quad (1)$$

Even though early satellite-based studies demonstrated a strong correlation between SIF and gross primary productivity (GPP; e.g., Guanter et al., 2014; Sun et al., 2018; Zhang et al., 2016), it has been shown that under certain conditions, SIF does not exhibit a linear relationship with GPP. For example, SIF inadequately represents the saturation in GPP under high light conditions (Kim et al., 2021; Liu et al., 2022; Zhang et al., 2016), and under severe environmental stress the relationship can completely break down (Martini et al., 2022; Wieneke et al., 2022; Wieneke et al., 2018; Wohlfahrt et al., 2018; Xu et al., 2021). The non-linear SIF-GPP relationship can be explained by three main factors:

i) the decoupling of *APAR* with SIF and GPP when light is not the limiting factor for PQ. It is well known that *APAR* is the main driver of the GPP-SIF relationship (Dechant et al., 2020; Miao et al., 2018; Wieneke et al., 2018; Yang et al., 2018). Under increased stress conditions, such as drought or nutrient limitation, the relationship between *APAR* and both SIF and GPP may be decoupled because the availability of light ceases to be the limiting factor for photosynthesis. Under those conditions, other factors such as water or nutrient availability and morphological changes become more important (Wang et al., 2023b; Wieneke et al., 2022; Wohlfahrt et al., 2018; Xu et al., 2021).

ii) the confounding effect of canopy structure (e.g., leaf angle) and leaf biochemical properties (e.g., chlorophyll *a*&b, carotenoids). Drought and heat stress can cause changes in the physiology and morphology of plants, which can affect the orientation of leaves. Under conditions of drought and heat stress, leaf angle may become closer to the vertical, which can help to reduce water loss by limiting the amount of direct sunlight that reaches the surface of the leaves (Barrs and Weatherley, 1962). In addition, nutrient limitation can also affect the concentration of chlorophyll (C_{ab}) in the leaves. Changes in C_{ab} concentration can alter the scattering and reabsorption properties of the canopy and, consequently, the amount of fluorescence photons detected by a sensor is affected by changing scattering and reabsorption properties and thereby altering f_{esc} (Dechant et al., 2020; Hwang et al., 2023; Wang et al., 2023b; Xu et al., 2021).

iii) the non-monotonic relationship Φ_F and Φ_{PQ} with increasing Φ_{NPQ}. While there is a clear negative linear relationship between Φ_{NPQ} and Φ_{PQ}, the relationship between Φ_F and Φ_P is more complex and mainly depends on Φ_{NPQ} (Porcar-Castell et al., 2021; Porcar-Castell et al., 2014). When Φ_{NPQ} is low (e.g., under low stress and low light conditions) Φ_F and Φ_P show a negative linear relationship. With increasing Φ_{NPQ} the relationship between Φ_F and Φ_P becomes positive since most energy is dissipated as heat. Under severe stress (photoinhibition), with highest values of Φ_{NPQ}, the relationship between Φ_F and Φ_P becomes negative again since only a limited amount of energy is used for PQ (Magney et al., 2019; van der Tol et al., 2014; Wieneke et al., 2022).

To interpret the physiologically-driven changes in SIF and to accurately understanding the relationship between F_{red} and $F_{far\text{-}red}$ under different stressors (Jonard et al., 2020), especially when measured at the canopy level and above, it is crucial to downscale SIF to photosystem level (i.e., estimating Φ_F) by removing the biochemical and structural confounding factors. The coarse spatial and temporal resolution of satellite-based SIF products, however, can make it difficult or impossible to measure these factors and cope with the non-linear response curves. In-situ observations are thus essential to develop new methods that allow for downscaling and signal interpretation. For each wavelength (λ) $\Phi_{F(\lambda)}$ can be calculated as:

$$\Phi_{F(\lambda)} = \frac{SIF(\lambda)}{APAR \bullet f_{esc}(\lambda)} \quad (2)$$

Where f_{esc} is dependent on wavelength-specific effects, such as reabsorption effects which dominate in the red spectral region and scattering effects prevailing in the far-red region. Radiative transfer models like SCOPE (Soil Canopy Observation, Photochemistry and Energy; van der Tol et al. (2009) and Yang et al. (2021) can be used to estimate f_{esc} for both individual leaves and the overall canopy. This is done by simulating the emission of SIF, as well as the absorption and scattering of radiation at these levels. In SCOPE, f_{esc} depends on the biophysical properties of the leaf (common to all leaves) and the spectral nature of the absorbed light, which varies with each canopy layer and discrete leaf angle. The applicability of these models is therefore often limited by the requirement of extensive sets of input variables that cannot always be measured during experiments.

Hence, reflectance based correction approaches are desirable. Zeng et al. (2021, 2019) and Yang et al. (2020) have previously demonstrated that f_{esc} of $F_{far\text{-}red}$ can be estimated by using a combination of visible (VIS) and near-infrared (NIR) reflectance factors to minimise scattering effects. Since these correction methods are based on the common VIS and NIR bands, they can be easily applied at different scales. However, estimating f_{esc} of F_{red} using the reflectance remains a challenge. While Romero et al. (2018, 2020) introduced a scaling factor to calculate the likelihood of F_{red} escaping from the leaf to the canopy, they acknowledge that their method is restricted to fluorescence generated by light-emitting diode (LED) or Light Amplification by Stimulated Emission of Radiation (LASER). Consequently, their correction is limited to active fluorescence measurements only. Liu et al., 2019b proposed a method based on a random forest algorithm trained on simulated data to scale red fluorescence from the canopy to the photosystem. Liu et al. (2020) later suggested a simpler alternative that uses red reflectance, the normalized difference vegetation index (*NDVI*) and the fraction of absorbed *PAR* by green leaves ($fAPAR_{green}$) to estimate $f_{esc,687}$ at the canopy level. For the correction of $f_{esc,687}$ at leaf level, Gitelson et al. (1998) and Van Wittenberghe et al. (2021) suggested two simple correction method based on the reflectance and transmittance in the red spectrum.

The overall aim of the study was to determine whether fluorescence signals and derived parameters can be used as reliable indicators of plant stress, particularly under heat and drought conditions. To investigate the effects of drought and heat stress on SIF, we conducted a mesocosm manipulation experiment with *Solanum tuberosum* 'Nicola' (potatoes). Because of their shallow root system, potatoes are known to be particularly vulnerable to heat and drought stress (Monneveux et al., 2013), which makes them a suitable subject for this study. For this, we set the following objectives: i) to compare the $f_{esc,687}$ models proposed by Gitelson et al. (1998), Van Wittenberghe et al. (2021) and Liu et al. (2020) with SCOPE simulations; ii) to adjust the existing leaf and canopy models if they are unable to effectively account for reabsorption effects; iii) to test the comparability of leaf and canopy measurements of F_{687}, F_{760}, $F_{687,PS}$ and $F_{760,PS}$ based on the best performing leaf and canopy models of $f_{esc,687}$; iv) to analyse the responses of leaf and canopy $\Phi_{F,687}$ and $\Phi_{F,760}$ to increasing heat and drought stress, v) to assess the variability of canopy $\Phi_{F,687}$ and $\Phi_{F,760}$ due to changes in the solar incidence angle.

2. Methods

2.1. Experimental setup

The study site was located at the Experimental site on the Drie Eiken Campus of the University of Antwerp in Belgium, situated at 51°09′ N, 04°24′ E. The experiment consists of ten mesocosms with five control and five drought treatments. Each mesocosm was 100 cm high, has a diameter of 50 cm and was placed under a transparent shelter to exclude natural wetting (Fig. A.1). The control mesocosms were regularly watered with tap water. The soil used in the experiment was a mixture of loamy soil and river sand, with an average texture of 80.8% sand, 0.8% clay, and 18.4% silt. The volumetric water content at 30 cm depth was continuously measured using the reflectometer CS616 (Campbell Scientific, Inc., Logan, USA). On May 21st, 2019, three *Solanum tuberosum* 'Nicola' potatoes were planted per mesocosm, and they were harvested on August 27th, 2019. Each mesocosm received 60 g of NPK fertilisers (5–4–15 + Bacillus). The mesocosms were placed on movable plates to allow for unobstructed clear sky measurements outside of the shelter. For more detailed information on the soil conditions, we refer to Vienne et al. (2022).

Leaf and canopy hyperspectral measurements were conducted with the hyperspectral Fluorescence Box (FloX, JB Hyperspectral Devices, Düsseldorf, Germany). The FloX comprises two spectrometers, FLAME and QEPro (both Ocean Optics, USA). FLAME has a spectral range of 400 to 950 nm with a spectral resolution of 1.5 nm full width at half maximum (FWHM) and a SNR of 250. QEPro is optimized for deriving SIF, with a spectral range of 650–800 nm, a FWHM of 0.3 nm, and an SNR of around 1000. Radiometric calibration was performed with the ISS-17-VA-V01 Integrating Sphere (GigaHertz Optic, Germany) at the JB Hyperspectral optical facility. A single measurement cycle lasts between 20 and 40 s and includes the following sequence: signal optimization for both channels (aiming at 80% coverage of the dynamic range), upward measurement, downward measurement, upward measurement, dark current measurements for both the upward and downward channels. The dark current correction is implemented in the FloX processing tool (Julitta, 2017; Julitta et al., 2017). Canopy SIF retrievals were performed using the QEPro spectrometer mounted on a 2-m-high tower and positioned in NADIR over the corresponding mesocosm. The field of view (FOV) of the downward looking optic is 23°, while the upward looking optic uses a cosine corrector (CC-3, Ocean Optics, USA) with a hemispherical view (180°). To minimise stray light effects on the canopy measurements, a 2 × 2 m black surface was placed under the canopy spectrometer.

Leaf measurements of SIF were conducted using the FLAME spectrometer with the FluoWat leaf clip (for a detailed description c.f. Van Wittenberghe et al., 2019). This allowed a near simultaneous measurement of the leaf and canopy signal within 10 to 30 s. The FluoWat has been designed to enable the observation of leaves from both upward and downward positions, with the light source falling on the leaf at a 45-degree angle. Reflectance (*R*) and transmittance (*T*) factors were measured using upward and downward fibre-optic insertions of the FLAME. Two short-pass filters that block light at wavelengths >650 nm and > 675 nm can be moved in front of the incident light to block incoming and consequently reflected light at the respective wavelengths. This provides upward and downward emitted SIF between 650 (675) to 800 nm (Van Wittenberghe et al., 2019; Van Wittenberghe et al., 2015; Van Wittenberghe et al., 2013). Due to the fact that FluoWat measurements require direct sunlight, the measurements were carried out exclusively during clear sky conditions and two to three hours around solar noon. Between June 28 and July 24, 2019 (Fig. 1), the ten mesocosms were measured around three times resulting in 32 measurements, with four leaf and 16 canopy measurements conducted for each mesocosm. The measurement cycle for a single mesocosm was carried out as follows:

I. The mesocosm was moved from its sheltered location to a 2 × 2 m black surface positioned beneath the spectrometer (c.f. Fig. A.1).
II. A white reference measurement was taken for the FluoWat and the FLAME spectrometer.
III. The FluoWat was then placed on a leaf and a FLAME measurement was taken without the low pass filter while the QEPro measured the potato canopy simultaneously.
IV. Measurements were then taken sequentially with the 650 nm filter and the 675 nm filter while the QEPro measured the potato canopy.
V. The mesocosm was then rotated by 90° and steps 2 to 5 were repeated three times until the mesocosm returned to its original position.

As a result of this measurement cycle, approximately 130 leaf-level and 520 canopy-level measurements were obtained for the entire campaign.

2.2. Separation into stress groups

We categorised the irrigated and control treatments into three stress groups (G1, G2, G3) based on the relative extractable water (*REW*) and vapour pressure (*VPD*; kPa), recognizing that plant drought stress is not solely determined by soil water availability (Bartlett et al., 2012). Fig. 1b shows the amount of measured mesocosm per stress group and campaign day. *VPD* was calculated as:

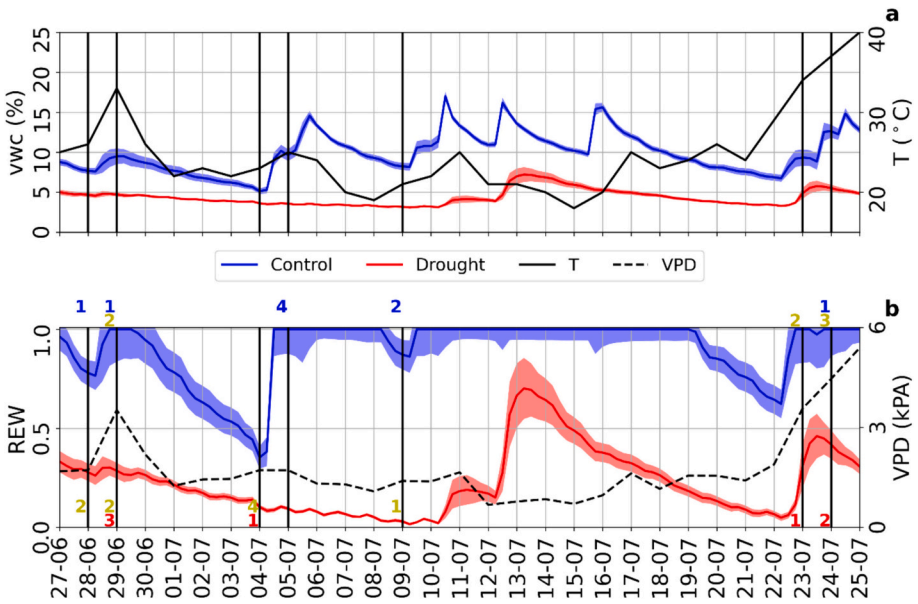

Fig. 1. Time series of environmental conditions over the seven campaign days indicated by the black vertical lines. The volumetric water content (vwc) and relative extractable water (REW) for the control and drought treatments are depicted by blue and red lines, respectively. The dashed line represents the vapour pressure deficit (VPD) at the study site. The amount of measured mesocosm at each campaign day are given by the coloured numbers (blue: stress group 1, yellow: stress group 2, red: stress group 3). Numbers close to the blue line indicate the stress group for control group, numbers close to the red line indicate the stress group for drought group. (For interpretation of the references to colour in this figure legend, the reader is referred to the web version of this article.)

$$VPD = e_s \bullet \left(\frac{100 - rh}{100}\right) \tag{3}$$

Where *rh* is the measured relative humidity (%) and e_s the saturation vapour pressure (hPa) and calculated by the Clausius-Clapeyron relation:

$$e_s = e_s(T_0) \bullet exp\left(\frac{L}{R_v}\left(\frac{1}{T_0} - \frac{1}{T}\right)\right) \tag{4}$$

Where $e_s(T_0)$ (6.11 hPa) is the saturation vapour pressure at the reference Temperature T_0 (273.15 K), L is the latent heat of evaporation for water (2.5×10^6 J kg^{-1}), R_v is the gas constant for water vapour (461 J K^{-1} kg^{-1}) and T the measured air temperature (K). López et al. (2021) conducted a meta-analysis involving 112 plant species to investigate the impact of increased *VPD* on plant physiology. The study revealed that when *VPD* values exceed 1.4 to 1.6 kPa, there was a decline in photosynthetic rates due to stomatal closure.

The relative extractable water (*REW*) represents the amount of water available for the plant and is calculated as:

$$REW = \frac{(vwc - wp)}{(fc - wp)} \tag{5}$$

Where *vwc* is the measured volumetric water content at a depth of 30 cm (%), *wp* is the wilting point and *fc* the field capacity. The wilting point is the volumetric water content at which plants cannot extract water from the soil, and as a result, they start to wilt and eventually die. The field capacity describes the maximum amount of water that the soil can hold against the force of gravity. We obtained both *wp* and *fc* from soil water retention curves, which were constructed based on *pF* values derived from laboratory analysis of soil samples. Many studies suggest that if the *REW* falls below 0.4, it indicates the occurrence of water supply stress (Sadras and Milroy, 1996; Vilhar, 2016).

To account for possible mixed environmental effects (e.g., low *VPD* and low *REW* or high *VPD* and high *REW*) we ordered the treatments into stress groups. Group one (G1) comprises measurements influenced by concurrent moderate *REW* (≥0.4) and low *VPD* (≤1.4 hPa), as well as concurrent high *REW* (≥0.6) and high *VPD* (≤2.5 hPa). Group three (G3) includes measurements affected by simultaneous high *VPD* (≥1.4 hPa) and low *REW* (≤0.15), as well as very high *VPD* (≤3.0 hPa) and high *REW* (≥0.75). Group two (G2) encompasses measurements not categorised in G1 and G3, characterised by low *REW* and low to medium *VPD* (Fig. 2).

2.3. Sun-induced fluorescence and reflectance indices

As described in chapter 2.1 leaf and canopy radiances were measured with the FloX system. Adaxial and abaxial leaf SIF were derived from a combination of the FLAME spectrometer and the FluoWat low pass filters. To obtain the full spectra of SIF, two low pass filters were used to cut the incoming light at 650 nm and 675 nm, respectively. It is important to note that the FluoWat filter cuts a portion of the photosynthetic active radiation (PAR; 400–700 nm), which is used by plants for photosynthesis. Therefore, the derived SIF values may be lower than SIF under natural light conditions. The measurements were taken under clear sky conditions, two to three hours around solar noon, to ensure a relatively consistent light regime. Canopy SIF was retrieved from the O_2—B and O_2-A absorption bands at 687 and 760 nm, respectively, using the spectral fitting method (SFM) developed by Meroni et al. (2010) and the singular vector decomposition (SVD) developed by Guanter et al. (2013), which are both implemented in the FloX data processing GUI v30.3 (Julitta, 2017; Julitta et al., 2017). Here, we used the standard settings of the processing GUI. It was shown that SFM retrievals can be influenced by atmospheric distortion while Fraunhofer-based retrievals (like SVD) resist atmospheric impacts but are noisier (Chang et al., 2020). Even though we only conducted measurements under clear sky conditions and at a close distance from the canopy, we compared the SFM with the SVD method to test for possible atmospheric influences. We found a strong agreement between these two retrieval methods for the red fluorescence (Fig. A.2), albeit with a less robust agreement in the far-red region. Given the higher uncertainty associated with the SVD retrieval (c.f. horizontal error bars in Fig. A.2), we decided to proceed with the SFM-retrieved fluorescence values. Finally, we converted the fluorescence radiance values (mW $m^{-2}sr^{-1}nm^{-1}$) to irradiance (mW m^{-2} nm^{-1}) by multiplying by π.

To account for variations in light conditions and interpret changes in the SIF signal caused by heat or drought, SIF has to be normalized by

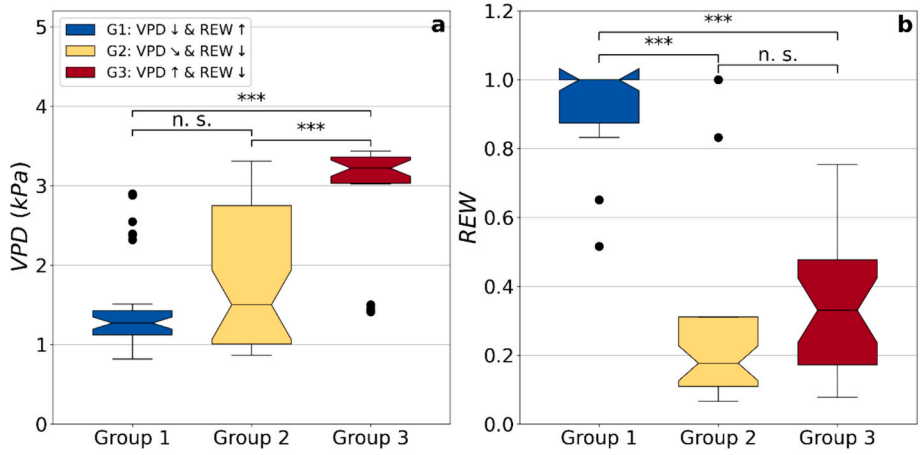

Fig. 2. Box plot distribution of vapour pressure deficit (a) and relative extractable water (b) after grouping. Group one (G1, blue boxes) comprises measurements affected by high REW values (≥0.4) and low VPD values (≤1.4 hPa). Group three (G3, red boxes) includes measurements influenced by high VPD values (≥1.6 hPa) and low REW values (≤0.2). Group two (G2, yellow boxes) encompasses all measurements not classified in G1 or G3 and is characterised by low REW and low to medium VPD values. The significant difference between each group are shown by the asterisk (ns = $P > 0.05$, *** = $P \leq 0.001$) above the box plots and were calculated by applying the Kruskal-Wallis significance test. The vertical line within the box plots represents the medians, the lower whiskers represent the first quartile, the upper whisker the third quartile, the black dots represent the outliers. (For interpretation of the references to colour in this figure legend, the reader is referred to the web version of this article.)

APAR (Dechant et al., 2020; Miao et al., 2018; Wieneke et al., 2018; Yang et al., 2018). *APAR* normalized SIF at a specific wavelength *(λ)* is often referred to as fluorescence yield or apparent fluorescence yield (FY_λ) and is calculated as:

$$FY_\lambda = \frac{SIF(\lambda)}{APAR_{chl}} \tag{6}$$

Furthermore, it is necessary to account for the fraction of *APAR* absorbed by chlorophyll *a*nd therefore, related to SIF. Hence, we calculated $APAR_{\mathrm{chl}}$ as:

$$APAR_{chl} = PAR \bullet fAPAR_{green} \tag{7}$$

Where *PAR* was measured by the BF5 pyranometer (Delta-T Devices, Cambridge, UK), the fraction of *PAR* absorbed by green leaves ($fAPAR_{green}$) was derived from the red edge *NDVI* ($NDVI_{RE}$) (Miao et al., 2018; Xu et al., 2021) as:

$$fAPAR_{green} = 1.37 \bullet NDVI_{RE} - 0.17 \tag{8}$$

The $NDVI_{RE}$ (Viña and Gitelson, 2005) was calculated as:

$$NDVI_{RE} = \frac{R_{750} - R_{705}}{R_{750} + R_{705}} \tag{9}$$

Where R_{750} and R_{705} are the canopy reflectance at 750 and 705 nm respectively. As SIF is strongly impacted by variations in the morphology of leaves and canopies, as well as changes in chlorophyll concentration. The normalisation by $APAR_{\mathrm{chl}}$ (c.f. Eq. *(6)*) does not entirely account for these effects (Porcar-Castell et al., 2021; Wang et al., 2023b; Xu et al., 2021), so that the so called escape probability ($f_{esc,\lambda}$) needs to be accounted for to derive fluorescence emission at the photosystem level ($F_{\lambda,\mathrm{PS}}$). The escape probability describes how structural and pigment effects influence the amount of photons which are actually detected by the sensor (Guanter et al., 2014). $F_{\lambda,\mathrm{PS}}$ is therefore calculated as:

$$F_{\lambda,PS} = \frac{F_\lambda}{f_{esc,\lambda}} \tag{10}$$

And consequently, the quantum use efficiency of fluorescence at the photosystem can be calculated as:

$$\Phi_{F,\lambda} = \frac{F_\lambda}{PAR \bullet fAPAR_{green} \bullet f_{esc,\lambda}} \tag{11}$$

Changes in the chlorophyll concentration were approximated by the MERIS Terrestrial chlorophyll index (*MTCI*; Dash and Curran (2004)):

$$MTCI = \left(\frac{R_{753.75} - R_{708.75}}{R_{708.75} - R_{681.25}}\right) \tag{12}$$

Where $R_{753.75}$, $R_{708.75}$ and $R_{681.25}$ correspond to the reflectance at 753.75, 708.75 and 681.25 nm respectively.

2.4. Estimation of $f_{esc,760}$ from reflectance data

Previous studies showed that the Fluorescence Correction Vegetation Index (*FCVI*) by Yang et al. (2020) and the Near-Infrared Reflectance of vegetation (NIR_{v}) (Zeng et al., 2019) can be used to estimate f_{esc} of F_{760}. As our measurement setup did not provide the full visible irradiance spectra required by the *FCVI*, we applied only the correction method proposed by Zeng et al. (2019). The NIR_{v} was calculated as:

$$NIR_v = \frac{R_{NIR} - R_{red}}{R_{NIR} + R_{red}} \bullet R_{NIR} \tag{13}$$

Where R_{NIR} and R_{red} is the reflectance in the NIR and red bands respectively. The escape probability of far-red fluorescence can then be approximated as:

$$f_{esc,760} \approx \frac{NIR_v}{fAPAR_{green}} \tag{14}$$

Analog to Eq.(10) $F_{760,\mathrm{PS}}$ was calculated as:

$$F_{760,PS} = \frac{F_{760}}{f_{esc,760}} \tag{15}$$

By rearranging Eq. (11) and (14) $\Phi_{\mathrm{F},760}$ can be calculated as:

$$\Phi_{F,760} = \frac{F_{760}}{PAR \bullet NIR_v} \tag{16}$$

It is important to note that NIR_v-based $f_{\mathrm{esc},760}$ can only be used to minimise scattering effects on far-red fluorescence since it assumes leaf albedo approximates to 1 (Zeng et al., 2019) and is therefore not suitable to estimate the escape probability of red fluorescence.

2.5. Estimation of $f_{esc,687}$ by SCOPE

The SCOPE model simulates radiative transfer processes and is

therefore commonly used to aid in the development of a reflectance-based empirical model to correct for fluorescence reabsorption. Our objective was to use SCOPE to estimate plausible foliar and structural parameters (c.f. Table 1) and reproduce fluorescence emission at both leaf and canopy scales by adjusting the quantum efficiency of each photosystem ($f_{qe,PSI}$ and $f_{qe,PSII}$) (Fig. 3). First, we employed the leaf RTM (Vilfan et al., 2018) and Bidirectional Reflectance Distribution Function (Bousquet et al., 2005) models to restrict the foliar radiative transfer parameters (such as N, C_{ab}, C_{ca}, C_{ant}, C_s, C_w, C_{dm}) using leaf transmittance and reflectance factors measured with the FluoWat. Subsequently, we inverted Fluspect, the leaf radiative transfer model in SCOPE, against abaxial and adaxial fluorescence radiances to get a first estimate of $f_{qe,PSI}$ and $f_{qe,PSII}$. Note that we consider the optimized f_{qe} as "effective" terms since they account for the physiological scaling of fluorescence. This is a common practice when incomplete information prevents the simulation of energy balance and photosynthesis processes with SCOPE (e.g., Celesti et al., 2018).

Afterwards, we computed the average foliar parameters for each pot, using four leaves per mesocosm. The reflectance factors obtained from FloX were then used to constrain Leaf Area Index (LAI) and Leaf Inclination Distribution Function ($LIDF_a$) using the coupled Fluspect-RTMo models of SCOPE ($LIDF_b$ was set to 0). Subsequently, we constrained f_{qe} assuming that only the rate of PSII would vary across the canopy, while a single effective $f_{qe,PSI}$ would suffice to represent both leaf and canopy fluorescence emission, as suggested by Porcar-Castell et al. (2021). To develop an empirical re-absorption approach, we created look-up tables comprising leaf-level simulations (FluoWat) and canopy-level simulations (FloX). These tables were generated by replicating the meteorological and observational conditions specific to each observation day. We used the vegetation parameters obtained through the inversion of SCOPE, while systematically varying C_{ab} values from 1 to 100 in increments of 2.5 μg cm^{-2}. This approach allowed to generate spectral indices, optical properties (such as transmittances), and fluorescence emissions at various spatial scales (including photosystem, leaf surface, and top of the canopy) along a C_{ab} gradient. These simulations were crucial for the development and testing of our approach. It is worth noting that due to limited information available on meteorological conditions, soil properties, and vegetation parameters, we relied solely on radiative transfer models for this purpose.

Table 1
Estimated leaf and canopy parameters by SCOPE. fqe,PSI and fqe,PSII,leaf and fqe,PSII,canopy were estimated as "effective" model parameters.

Parameter	Retrieved mean and range	Symbol	Units
Leaf chlorophyll content	23.57 ∈ [16.61, 28.44]	C_{ab}	μg cm^{-2}
Leaf carotenoids content	4.56 ∈ [3.8611, 5.1623]	C_{ca}	μg cm^{-2}
Leaf anthocyanins content	1.6981 ∈ [0.794, 2.694]	C_{ant}	μg cm^{-2}
Leaf senescent pigments content	0.0174 ∈ [0.0000, 0.1887]	C_s	a.u.
Leaf water content	0.0120 ∈ [0.0040, 0.0760]	C_w	g cm^{-2}
Leaf dry matter content	0.0019 ∈ [0.0019, 0.0019]	C_{dm}	g cm^{-2}
Leaf structural parameter	1.567 ∈ [1.459, 1.68]	N	layers
Leaf area index	2.334 ∈ [1.809, 3.179]	LAI	m^2 m^{-2}
Leaf inclination distribution function	−0.042 ∈ [−0.637, 1.000]	$LIDF_a$	–
Photosynthetic quantum efficiency of photosystem I	0.0137 ∈ [0.0078, 0.0183]	$f_{qe,PSI}$	–
Photosynthetic quantum efficiency of photosystem II at leaf level	0.0067 ∈ [0.0058, 0.0099]	$f_{qe,PSII,leaf}$	–
Photosynthetic quantum efficiency of photosystem II at canopy level	0.0137 ∈ [0.0078, 0.0183]	$f_{qe,PSII,canopy}$	–
Solar zenith angle		θ_{sun}	Deg

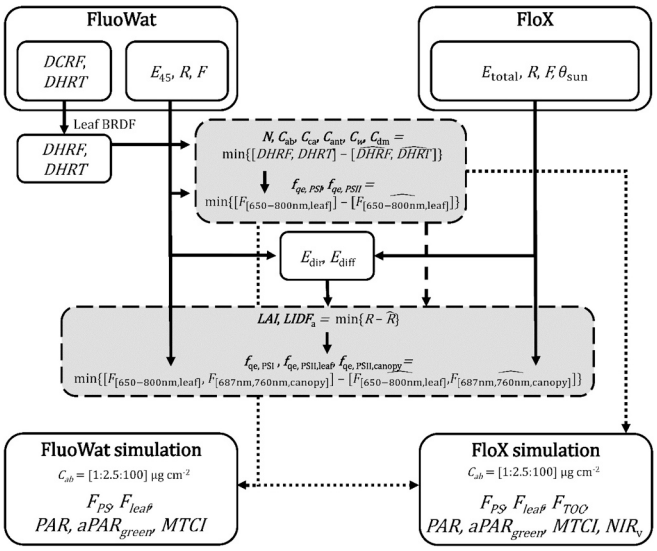

Fig. 3. Flowchart of the SCOPE data assimilation scheme. The Fluspect model and the FluoWat measurements were used to constrain foliar biophysical parameters accounting for leaf bi-directional reflectance function and the instrument illumination conditions. Then leaf fluorescence quantum efficiency was constrained for each photosystem against fluorescence radiances. Similarly, SCOPE model was used to constrain structural parameters and then fluorescence quantum efficiency of photosystem I and a canopy and leaf level quantum efficiencies of photosystem II were constrained against FloX and FluoWat fluorescence radiances, simultaneously. These parameters and the measurement conditions were used to simulate spectral variables at leaf and canopy level. Large solid-line boxes represent observed or simulated datasets. Small solid-line boxes and arrows represent observed variables that are passed along the processing. Dashed-line grey boxes represent the retrieval of leaf and canopy variables via SCOPE model inversion, and the dashed arrows represent these variables being passed to further steps of the process.

Fig. 3 summarizes the SCOPE model inversion. FluoWat and FloX spectral measurements were aggregated for each sample. We used the leaf bidirectional reflectance distribution function model developed by Bousquet et al. (2005) and corrected by Stuckens et al. (2009) to subtract the specular reflected component from the directional-conical reflectance factors ($DCRF$). We assumed that the specular component did not interact with the leaf and considered the transmittance factor as directional-hemispherical ($DHTF$). Subsequently, we used the Fluspect model (Vilfan et al., 2016, 2018) to invert the model against directional-hemispherical reflectance factors ($DHRF$) and $DHTF$ in order to constrain the foliar radiative transfer parameters (N, C_{ab}, C_{ca}, C_{ant}, C_s, C_w, C_{dm}) for each sample. In the next step, we constrained a first guess of leaf $f_{qe,PSI}$ and $f_{qe,PSII}$ by inverting the model against abaxial and adaxial fluorescence radiances. Throughout these steps, we eliminated the incoming irradiance absorbed by the low pass filter of FluoWat from the measurements when applicable.

Before transitioning to the canopy level, it was necessary to enhance the representation of illumination. While SCOPE calculates default down-welling direct and diffuse irradiances using integrated short and longwave radiation, we lacked those measurements. However, we had access to the incoming irradiance data obtained from FloX, solar zenith angle, and direct irradiance at 45° measured with FluoWat. To estimate the direct and diffuse components of incoming irradiance, we assumed that atmospheric conditions remained relatively constant between leaf and canopy measurements. Additionally, we presumed that the FluoWat measured only direct irradiance. Based on this assumption, we estimated the direct irradiance by correcting the FluoWat irradiance (measured at 45° relative to the white reference) using the ratio of illumination angle cosines: $E_{canopy,\theta_{sun}} = E_{FluoWat,45} \bullet cos(\theta_{sun})/cos(45)$. We then subtracted

the estimated direct irradiance from the total spectral irradiance to calculate the diffuse irradiance. The estimated foliar parameters were averaged per pot, considering four leaves per plant. We estimated the LAI and LIDFa by inverting the coupled Fluxpect-RTMo models of SCOPE against the FloX reflectance factors. However, due to variations in photosynthetic rates, particularly in terms of illumination, the fluorescence measured by FluoWat was not representative of the entire canopy or the signal observed at the top of the canopy. As a result, it was not possible to directly match the fluorescence radiances at the top of the canopy using the previously estimated f_{qe} values.

Based on the understanding that Photosystem I (PSI) is less susceptible to down-regulation, we assumed that a single effective $f_{qe,PSI}$ value could adequately represent both leaf-level and canopy-level fluorescence emissions (Porcar-Castell et al., 2021). However, for Photosystem II (PSII), we distinguished between the estimates at the leaf level ($f_{qe,PSII,leaf}$) and at the canopy level ($f_{qe,PSII,\ canopy}$). This differentiation acknowledges the potential differences in PSII behaviour and response between individual leaves and the entire canopy. We employed the top of the canopy fluorescence radiance estimates in the O_2-A and O_2—B bands, as well as the abaxial and adaxial fluorescence radiances from FluoWat, to constrain $f_{qe,PSI}$, $f_{qe,PSII,leaf}$, and $f_{qe,PSII,canopy}$. The leaf-level estimates of $f_{qe,PSI}$ and $f_{qe,PSII}$ served as the initial values for the model inversion. Using these fluorescence measurements allowed to refine the estimation of $f_{qe,PSI}$, $f_{qe,PSII,leaf}$, and $f_{qe,PSII,canopy}$ parameters.

To develop an empirical re-absorption approach, we generated look-up tables consisting of leaf-level simulations using FluoWat and canopy-level simulations using FloX. We ensured that the meteorological and observational conditions for each pot were accurately replicated in these simulations. We used the vegetation parameters obtained through the inversion of SCOPE, with varying Cab values ranging from 1 to 100 with increments of 2.5 μg cm^{-2}.

The FluoWat simulations provided fluorescence emission irradiances at the photosystem level, excluding internal re-absorption and scattering, as well as the averaged leaf forward and backward surface fluorescence irradiances, accounting for internal re-absorption and scattering. Based on these simulations, we calculated $APAR_{chl}$ to determine the corresponding fluorescence yields for the different fluorescence radiances. Additionally, we computed spectral indices (e.g., *MTCI*, NIR_v, or *NDVI*) and obtained leaf transmittance (*T*) and reflectance (*R*) factors.

To explore the effects of different C_{ab} values at canopy level, we followed a similar scheme for the FloX simulations. SCOPE provided fluorescence emission irradiances at the photosystem and leaf surface levels, both without and with internal re-absorption and scattering, as well as the top of the canopy fluorescence radiance in the observation direction. We calculated the total $APAR_{chl}$ irradiances to determine the respective yields, along with *MTCI*, NIR_v and *NDVI*. The canopy transmittance was computed as the ratio of the top of the canopy irradiance and the down-welling irradiance below the bottom layer of the canopy.

2.6. Estimation of $f_{esc,687}$ from reflectance data

As red SIF is partly reabsorbed within the leaf and through the canopy, F_{687} emitted at the chloroplast is higher than F_{687} detected above the canopy (Lichtenthaler and Rinderle, 1988; Romero et al., 2020; Van Wittenberghe et al., 2021). If chlorophyll concentration (C_{ab}) decreases, fewer red photons are absorbed and reabsorbed by the leaf and canopy (*Fig. A.3a*). As a result, under lower C_{ab}, the sensor is able to detect more photons, leading to an increase in $f_{esc,687}$ (*Fig. A.3b*) and consequently F_{687} at leaf and canopy (Rossini et al., 2015; Van Wittenberghe et al., 2013). In this study, we evaluate reflectance-based models of $f_{esc,687}$ ($f_{esc,687,RS}$) in comparison to SCOPE-derived $f_{esc,687}$ ($f_{esc,687,SCOPE}$) at both leaf and canopy levels. We applied the models proposed by Gitelson et al. (1998) and Van Wittenberghe et al. (2021) at leaf level, including a modification of the latter described below. For canopy $f_{esc,687,RS}$, we tested the model proposed by Liu et al. (2020) and two modified versions of it. To enable a comparison of these models across broader C_{ab} values, we linearly adjusted the value range of the $f_{esc,687,RS}$ models based on the C_{ab} gradient simulated by SCOPE (c.f. section 2.5). Thus, $f_{esc,687,RS,adj}$ was calculated as:

$$f_{esc,687,RS,adj} = f_{esc,687,RS} \bullet a + b \tag{17}$$

Where the regression coefficients a and b were derived from the relationship of $f_{esc,687,SCOPE}$ and the respective model for $f_{esc,687,RS}$ along the simulated C_{ab} gradient (c.f. Table A.1). The predictive power of the proposed models was assessed by the coefficient of determination (R^2) between $f_{esc,687,SCOPE}$ *and* $f_{esc,687,RS}$ for the modelled C_{ab} gradient and measured values.

2.6.1. Leaf level

At the leaf level, Gitelson et al. (1998) suggested a simple wavelength-dependent correction function to estimate $f_{esc,687}$ at 687 nm as:

$$f_{esc,687,git} \approx R_{687} + T_{687} \tag{18}$$

With the general assumption that the non-absorbed radiation at a given wavelength linearly correlates with the escape probability of fluorescence at the given wavelength (here 687 nm) (*Fig. A.3a&b*). While we find a strong to moderate squared Pearson correlation coefficient (r^2) between the sum of R_{687} and T_{687} and the $f_{esc,687}$ derived from SCOPE ($f_{esc,687,SCOPE}$) at leaf and canopy level ($r^2 = 0.82$ and 0.67, respectively), a non-linear relationship persists as shown in *Fig. A.3c*. We adjusted for this non-linearity by taking the square root of $f_{esc,687,git}$, as:

$$f_{esc,687,git,mod} = \sqrt{f_{esc,687,git}} \tag{19}$$

Which resulted in an improved r^2 value of 0.94 for leaf and 0.83 for canopy (*Fig. A.3d*). Van Wittenberghe et al. (2021) proposed an improved approach of Gitelson et al. (1998), by normalising leaf measured F_{687} by adaxial and abaxial leaf reflectance and transmission respectively:

$$F_{687,PS} \approx \frac{F_{up,687}}{R_{687}} + \frac{F_{dw,687}}{T_{687}} \tag{20}$$

Where $F_{687,PS}$ is the F_{687} emission at the photosystem, $F_{up,687}$ and $F_{dw,687}$ represent the F_{687} emission in the adaxial and abaxial directions, respectively. The corresponding escape probability can be approximated by reformulating Eq. *(10)* to:

$$f_{esc,687,wit} \approx \frac{F_{up687} + F_{dw,687}}{F_{687,PS}} \tag{21}$$

Given the improvement observed with $f_{esc,687,wit}$ over $f_{esc,687,git}$ ($R^2 = 0.84$ and $R^2 = 0.76$, respectively; Fig. 7a), we proceed with the model proposed by Van Wittenberghe et al. (2021). The correlation between $f_{esc,687,wit}$ and $f_{esc,687,SCOPE}$ was further improved (Fig. 7a, black cross, $R^2 = 0.96$) by calculating the square root as done for the Gitelson et al. model:

$$f_{esc,687,wit,mod} = \sqrt{f_{esc,687,wit}} \tag{22}$$

Building upon the adjustments of $f_{esc,687,wit,mod}$ we calculated leaf $F_{687,PS}$ analogue to Eq. (12) as:

$$F_{687,PS} = \frac{F_{687}}{f_{esc,687,wit,mod}} \tag{23}$$

Following Eq. *(11)*, leaf $\Phi_{F,687}$ was calculated as:

$$\Phi_{F,687} = \frac{F_{687}}{PAR \bullet fAPAR_{green} \bullet f_{esc,687,wit,mod}} \tag{24}$$

2.6.2. Canopy level

Even though results showed that $f_{esc,687,git,mod}$ strongly correlates

with $f_{esc,687,SCOPE}$ (*Fig. A.3d*) it should be noted that T_{red} cannot be easily measured at canopy level and is therefore rarely available. Furthermore, the measured bidirectional R_{red} is influenced by both leaf and soil reflectance. Consequently, the soil background contribution, in particular under changing leaf inclination angles (*LIA*), needs to be taken into consideration. Fig. 4a demonstrates that the reflectance of the vegetation (R_{veg}) generally decreases as *LIA* increases. The contribution of the soil reflectance (R_{soil}) on the other hand, increases (Fig. 4b), leading to higher total reflectance (R_{total}), especially in the red wavelength region (620 to 700 nm; Fig. 4c). Liu et al. (2020) proposed an approximation of $f_{esc,687}$ at canopy based on the ratio of the reflected red light by the vegetation ($R_{red,veg}$) and $fAPAR_{green}$:

$$f_{esc,687,liu} \sim \frac{R_{red,veg,NDVI}}{fAPAR_{green}} \tag{25}$$

Based on PROSAIL model simulations, they determined that the contribution from the soil can be effectively compensated for by considering the square of the *NDVI*:

$$R_{red,veg,NDVI} \approx R_{red,total} \bullet NDVI^2 \tag{26}$$

Subsequently, $F_{687,PS,liu}$ was calculated analogously to Eq. *(23)*. After comparing leaf and canopy F_{687} and $F_{687,PS,liu}$ however, we found a worsening of the relationship (r^2: 0.3 to 0.2) after applying the correction method (c.f. Fig. A.4). We therefore tested how the relationship between $R_{red,veg}$ and $R_{red,tot}$ changes with increasing *LIA* and how well *NDVI*, the 2-band enhanced vegetation index (EVI2), NIR_v and the kernel *NDVI* (*kNDVI*) perform in estimating $R_{red,veg}$ (Fig. 5). We calculated the EVI2 based on Jiang et al. (2008) as:

$$EVI2 = 2.4\frac{R_{NIR} - R_{red}}{R_{NIR} + R_{red} + 1} \tag{27}$$

The kNDVI (Camps-Valls et al., 2021), which is a nonlinear generalization of the *NDVI* that is shown to propagates lower uncertainty and addresses saturation issues (Wang et al., 2023a), was calculated as:

$$kNDVI = \frac{1 - k(R_{NIR}, R_{red})}{1 + k(R_{NIR}, R_{red})} \tag{28}$$

The kernel function $k(R_{NIR},R_{red})$ measures the similarity between R_{NIR} *and* R_{red} and was calculated as:

$$k(R_{NIR}, R_{red}) = exp\left(-\frac{(R_{NIR} - R_{red})^2}{(2\sigma^2)}\right) \tag{29}$$

We fixed the length scale parameter σ, as described by Pabon-Moreno et al. (2022), to the median of the average value between R_{NIR} and R_{red}:

$$\sigma = median(0.5(R_{NIR} + R_{red})) \tag{30}$$

*Fig. 5*b&e show a non-linear relationship between $NDVI^2$ and the ratio of $R_{red,veg}$ to $R_{red,tot}$ resulting in a non-monotonic relationship of $R_{red,veg,NDVI}$ with SCOPE-derived $R_{red,veg}$. This relationship is only positive at low (<35°) and very high (>80°) *LIA*. While $EVI2^2$ improves upon $NDVI^2$, it still exhibits a non-linear relationship with the ratio of $R_{red,veg}$ to $R_{red,tot}$. Conversely, $kNDVI^2$ and NIR_v^2 demonstrate a stronger linear relationship with the ratio of $R_{red,veg}$ to $R_{red,tot}$, than $EVI2^2$ and $NDVI^2$, especially when *LIA* exceeds 45°. The highest r^2 values between $R_{red,veg,VI}$ and $R_{red,veg,simulated}$ as well as $R_{red,veg,retrieved}$ were found for *kNDVI* (r^2 = 0.99 and 0.80 respectively), closely followed by NIR_v (r^2 = 0.97 and 0.78 respectively). After testing the influence of changing *LIA* we analysed the robustness of *NDVI*, *EVI2*, *kNDVI* and NIR_v to a gradient in C_{ab} (Fig. A.5). While *NDVI*, *EVI2* and NIR_v showed very high r^2 values (0.94, 0.99, 0.94 respectively), kNDVI exhibited an oversensitivity in the low and high value ranges of the C_{ab} gradient, resulting in an r^2 of 0.81. Given the weak performance of *NDVI* and *EVI* in estimating $R_{red,veg}$ under changing *LIA* and the lower r^2 in estimating $R_{red,veg}$ with changing C_{ab} we replacing *NDVI* in Eq. *(26)* with NIR_v:

$$R_{red,veg,NIRv} \approx R_{red,total} \bullet NIR_v{}^2 \tag{31}$$

Analog to Eq. *(25)*, NIR_v based $f_{esc,687}$ was estimated as:

$$f_{esc,687,NIRv} \sim R_{red,veg,NIRv} fAPARgreen \tag{32}$$

To account for the abrupt decrease in $f_{esc,687}$ observed under low C_{ab} concentration (c.f. *Fig. A.3b* and Fig. A.5), we normalized by the square root of *MTCI* Dash and Curran (2004, 2007):

$$R_{red,veg,NIRv,MTCI} \approx \frac{R_{red,total} \bullet NIR_v{}^2}{\sqrt{MTCI}} \tag{33}$$

Analog to Eq. (25), NIR_v and *MTCI* based $f_{esc,687}$ was estimated as:

$$f_{esc,687,NIRv,MTCI} \sim \frac{R_{red,veg,NIRv,MTCI}}{fAPAR_{green}} \tag{34}$$

Building upon the improvement of $f_{esc,687,NIRv,MTCI}$ shown in (Fig. 7b&c) we calculated canopy $F_{687,PS}$ analogue to Eq. *(10)* as:

$$F_{687,PS} = \frac{F_{687}}{f_{esc,687,NIRv,MTCI}} \tag{35}$$

Following Eq. *(11)*, canopy $\Phi_{F,687}$ was calculated as:

$$\Phi_{F,687} = \frac{F_{687}}{PAR \bullet fAPAR_{green} \bullet f_{esc,687,NIRv,MTCI}} \tag{36}$$

2.7. Analysing the impact of mesocosm rotation on red and far-red FY and Φ_F

As described in section 2.1 we rotated the mesocosms by 90° after four canopy measurements in one position were completed. To analyse the sensitivity of FY_{687}, F_{760}, $\Phi_{F,687}$ and $\Phi_{F,760}$ to changing solar incidence angle (Kreith and Kreider, 1978; Yang et al., 2023), we compared the variability of the measurements within a rotation state and between rotation states. Given that the measurements were taken under stable clear sky conditions, and each mesocosm was sampled within approximately 45 min, it is reasonable to assume that there were no substantial changes in the normalized responses (i.e., Φ_F) to environmental conditions. To quantify the variability of FY_{687}, F_{760}, $\Phi_{F,687}$ and $\Phi_{F,760}$ we

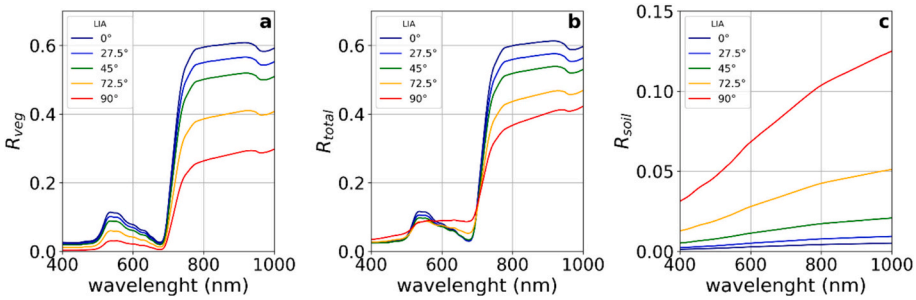

Fig. 4. SCOPE simulated canopy spectra under different leaf inclination angles.

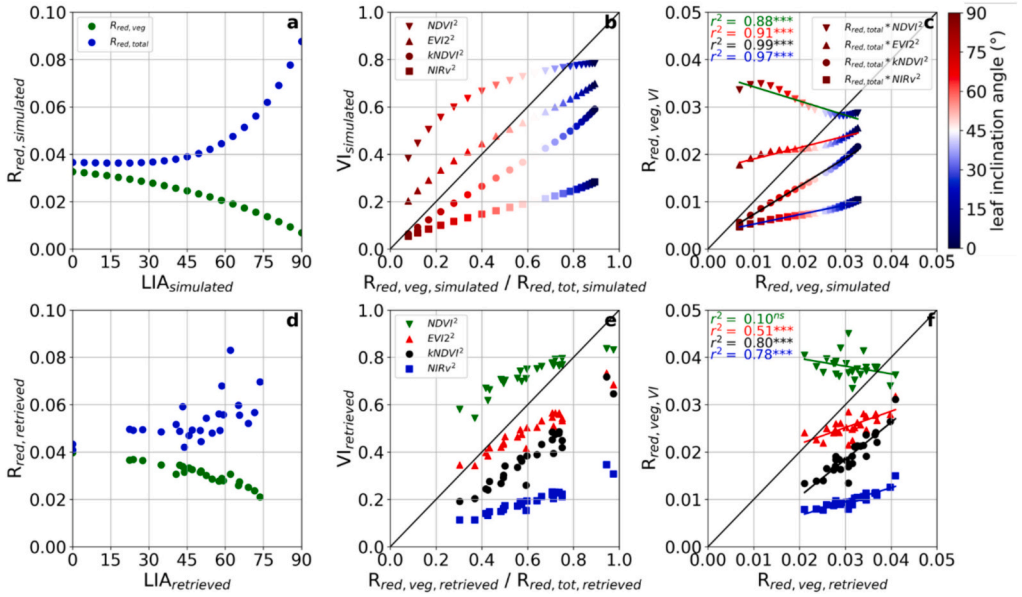

Fig. 5. Plot a,b,c show SCOPE simulated gradient in leaf inclination angle (LIA) and its impact on the red reflectance (R_{red}) and vegetation indices (VIs). Plot d, e, f show SCOPE retrieved R_{red} and VIs based on canopy measurements. a&d) Relationship between R_{red} from vegetation ($R_{red,veg}$; red dots) and R_{red} from vegetation and soil ($R_{red,tot}$; blue dots) with increasing LIA. b&e) Relationship between NDVI (normalized difference vegetation index, green inverted pyramid symbol), EVI2 (enhanced vegetation index 2, red pyramid symbol), kNDVI (kernel NDVI, black dots), NIRv (near infrared of vegetation, blue squares) and the ratio of $R_{red,veg}$ and $R_{red,tot}$. c&f) Relationship between $R_{red,veg}$ derived from VIs ($R_{red,veg,VI}$) and $R_{red,veg}$ derived from SCOPE ($R_{red,veg,simulated}$ & $R_{red,veg,retrieved}$). The squared Pearson correlation coefficient (r^2) is given with the significance level indicated by the asterisk (ns = $P > 0.05$, * = $P \leq 0.05$, ** = $P \leq 0.01$, *** = $P \leq 0.001$). (For interpretation of the references to colour in this figure legend, the reader is referred to the web version of this article.)

calculated the coefficient of variation (*CV*) as the ratio of their standard deviation and their mean within a rotation state and between rotation states (from here on referred to as $CV_{no\text{-}rotation}$ and $CV_{rotation}$). We calculated $CV_{no\text{-}rotation}$ from the four consecutive spectrometer measurements taken at a specific rotation angle and $CV_{rotation}$ from the averaged measurements obtained at each rotation angle. To quantify the impact of f_{esc} on the *CV*, we calculated the difference between the *CV* in Φ_F *(11)* and *FY (6)* for the respective wavelength at 687 and 760 nm.

2.8. Statistics

Data normality and homoscedasticity was tested by using Shapiro-Wilk and Levene tests, respectively. The best-fit parameters for the regression models were obtained using the technique of ordinary least-squares minimization. To compare the strength of the linear relationship between different variables we calculated the squared Pearson correlation coefficient (r^2). The coefficient of determination (R^2) was used to evaluate the predictive power of the empirical f_{esc} models with the process-based estimates by SCOPE. The Kruskal-Wallis significance test was applied for pairwise comparison to determine if there is a significant difference between our stress groups.

3. Results

3.1. Environmental conditions and phenological development

During the measurement campaign, which included seven days between June 27 and July 24, temperatures initially fluctuated between 20 and 25 °C. Notably, from July 21 to 25, there was a sharp temperature rise of over 40 °C (Fig. 1a), during which the highest *VPD* was also recorded (Fig. 1b). The relative extractable water (*REW*), derived at a depth of 30 cm, was maintained above 0.4 in the control group, while it remained most days below 0.4 in the drought treatments (Fig. 1b). It is worth noting that values above 0.4 in the drought treatments were only attained after watering (Fig. 1b red line). Both *MTCI* and $fAPAR_{green}$ decreased during the measurement period, with the greatest decline observed at the canopy level (Fig. 6a&*b*). Consequently, there was a corresponding decrease in $APAR_{chl}$, which persisted until the final days of the measurement campaign, at which point $APAR_{chl}$ slightly increased at the leaf level (Fig. 6c). It is worth noting that the canopy *MTCI* was higher for the drought treatments compared to the control group. It only dropped below the control group values during the severe drought towards the end of the campaign (Fig. 6a; 23–24 July). A similar trend was observed for $fAPAR_{green}$ and $APAR_{chl}$ (Fig. 6b&*c*).

3.2. Comparison of the reabsorption correction models

The leaf f_{esc} models proposed by Gitelson et al. (1998) ($f_{esc,687,git}$) and Van Wittenberghe et al. (2021) ($f_{esc,687,wit}$) showed R^2 of 0.76 and 0.84, respectively, across the modelled C_{ab} gradient (c.f. Fig. 7a&*c*). The $f_{esc,687,wit,mod}$ is very closely aligned with the 1:1 line, with a R^2 of 0.95 and the lowest relative root mean square error (*rRMSE*) of 6.2% (Fig. 7a). Within the measured value range of $f_{esc,687}$, both $f_{esc,687,git}$ and $f_{esc,687,wit}$ tend to be underestimated, leading to a negative R^2 and a high *rRMSE* exceeding 45%. In contrast, the $f_{esc,687,wit,mod}$ exhibited robust performance with R^2 of 0.94 and a low *rRMSE* of 5.1%. It is noteworthy that the squared Pearson coefficient (r^2) was very high (0.97) for all models (Fig. 7c).

Along the modelled C_{ab} gradient, $f_{esc,687,liu}$, $f_{esc,687,NIRv}$ and $f_{esc,687,NIRv,MTCI}$ have R^2 values of 0.92, 0.90 and 0.99 and *rRMSE* of 7.1%, 7.4% and 1.7%, respectively (Fig. 7b & d). Within the measured value range, we observed a negative, non-significant R^2 of −1.24 between $f_{esc,687,liu}$ and $f_{esc,687,SCOPE}$ (Fig. 7d). In contrast, $f_{esc,687,NIRv}$ and $f_{esc,687,NIRv,MTCI}$ exhibited robust performance with R^2 values of 0.67 and 0.70 and *rRMSE* of 16.3% and 15.7%, respectively.

3.3. Comparison of leaf and canopy fluorescence

In order to improve our understanding of leaf to canopy scaling and to test the efficiency of scattering and reabsorption correction, we compared uncorrected leaf and canopy F_{687} and F_{760} and with corrected $F_{687,PS}$ and $F_{760,PS}$. For the correction of leaf F_{687}, we used $f_{esc,687,wit,mod}$,

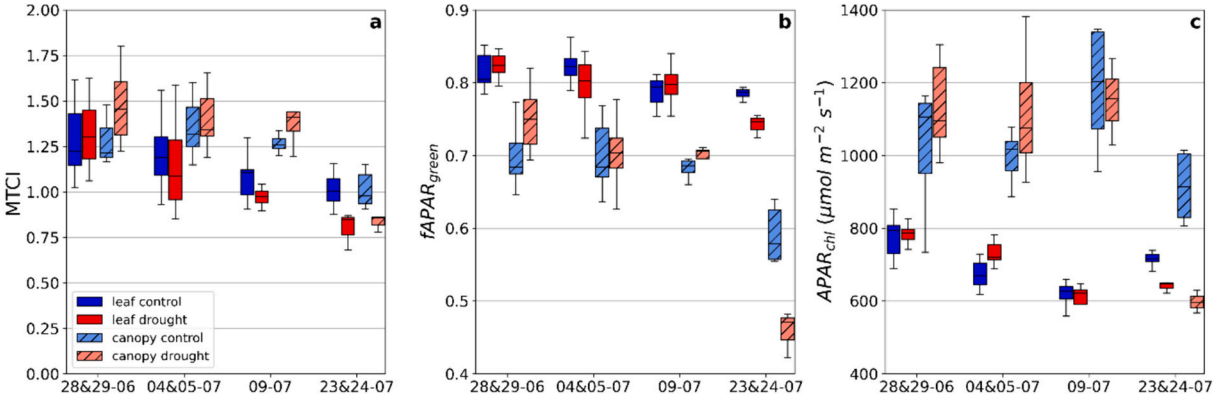

Fig. 6. The box plots illustrate the distribution of the MERIS terrestrial chlorophyll index (MTCI) (a), the fraction of absorbed photosynthetic active radiation by the leaves (fAPAR$_{green}$) (b), and the absorbed photosynthetic active radiation by chlorophyll (APAR$_{chl}$) (c) throughout the measurement campaign. The blue boxes represent the spread within the five control mesocosms, the red boxes represent the spread within the five drought mesocosms. All mesocosms were placed under a transparent shelter to exclude natural wetting. The control mesocosm were regularly watered with tap water. Non-hatched boxes indicate leaf-level measurements, while hatched boxes indicate canopy-level measurements. (For interpretation of the references to colour in this figure legend, the reader is referred to the web version of this article.)

while for correcting canopy F_{687}, we used $f_{esc,687,NIRv}$. It is important to note that the leaf and canopy values of fluorescence were retrieved using different methods and sensors, and thus are expected to be independent observations. The outlier, depicted by the red dot in Fig. 8a & c, exerted a strong influence on the overall r^2. This outlier comprises four leaf and 16 canopy measurements taken on July 24, a day characterised by exceptionally high *VPD* (>3.3 kPa). Although other mesocosm experienced similar high *VPD* levels, this particular mesocosm was impacted by low *REW* (<35%). It is worth noting that the outlier exhibited the highest values of leaf-level F_{687} and $F_{687,PS}$, while canopy F_{687} and $F_{687,PS}$ were at their lowest. Importantly, this effect was not observed for F_{760} and $F_{760,PS}$. When the outlier is excluded from the analysis of red fluorescence, we observed that canopy and leaf F_{687} and F_{760} showed a moderate relationship, with an r^2 value of 0.30 and 0.34, respectively (Fig. 8a&*b*). Upon correcting for reabsorption and scattering effects, we observed a strong improvement in the relationship between leaf and canopy $F_{687,PS}$ as well as between leaf and canopy $F_{760,PS}$, with r^2 of 0.50 and 0.48, respectively (Fig. 8c&*d*).

After demonstrating that the correction methods improved the relationship between canopy and leaf measurements, we evaluated the seasonal behaviour of $\Phi_{F,687}$ and $\Phi_{F,760}$. Fig. A.6 illustrates that both leaf $\Phi_{F,687}$ and $\Phi_{F,760}$ exhibit similar trends, displaying an increase until July 23rd and 24th, coinciding with temperatures exceeding 32 °C (c.f. Fig. 1), after which values decline. However, an exception is observed in leaf $\Phi_{F,687}$ of the drought treatments, where a substantial increase occurred on 23rd and 24th July. Canopy $\Phi_{F,687}$ and $\Phi_{F,760}$ on the other hand, exhibit markedly different patterns. While $\Phi_{F,687}$ remained relatively stable for both drought and control treatments, $\Phi_{F,760}$ showed a consistent decrease until July 23rd and 24th after which values began to increase.

Given that both the control and drought treatments are subject to rising temperatures, we assessed the behaviour of $\Phi_{F,687}$ and $\Phi_{F,760}$ under increasing soil and atmospheric drought conditions (c.f. Fig. 2). Fig. 9a illustrates that leaf and canopy Φ_{F687} significantly decreases with increasing stress. Although the significant level is lower, we observed the same pattern of decrease in leaf $\Phi_{F,760}$ with increasing stress (Fig. 9b). Canopy $\Phi_{F,760}$ values, on the other hand, show the lowest values and highest variance within the low stress group (G1), while a non-significant decrease in $\Phi_{F,760}$ values was observed from G2 to G3. This observation contrasts with all other measurements, indicating a unique response in canopy $\Phi_{F,760}$ under low stress conditions. To assess the influence of the retrieval method on our findings, we reproduced Fig. 9 but using the SVD retrieval method (c.f. Fig. A.7). Our results indicate that the SVD method yielded a similar pattern as observed with the SFM retrieval method, albeit with a greater spread (c.f. Fig. A.2), resulting in less pronounced and statistically significant differences.

3.4. Impact of the mesocosm rotation on FY_{687}, FY_{760}, $\Phi_{F,687}$ and $\Phi_{F,760}$

As described in section 2.7, we rotated the mesocosm four times by 90° to analyse the sensitivity of FY_{687}, FY_{760}, $\Phi_{F,687}$ and $\Phi_{F,760}$ to changes in solar incidence angle. We calculated the *CV* of the measurements within a rotation state and between rotation states ($CV_{no\text{-}rotation}$ and $CV_{rotation}$, respectively). We observed that the $CV_{no\text{-}rotation}$ and $CV_{rotation}$ were lower for FY_{687} compared to FY_{760} especially for G1. While $CV_{rotation}$ increased in FY_{687} with stress level, $CV_{no\text{-}rotation}$ and $CV_{rotation}$ of FY_{760} were high for G1 and G3 (*Fig. 10*a&b). $CV_{no\text{-}rotation}$ and $CV_{rotation}$ for $\Phi_{F,687}$ and $\Phi_{F,760}$ showed very similar patterns to those observed in FY_{687} and FY_{760}. However, $CV_{rotation}$ decreased for both $\Phi_{F,687}$ and $\Phi_{F,760}$ indicating a more consistent response across the mesocosms (Fig. 10c&*d*). Fig. 10e&*f* shows the change in *CV* resulting from the implementation of the respective correction methods. Negative values indicate an improvement, while positive values suggest a worsening. The correction methods had minimal impact on $CV_{no\text{-}rotation}$ but showed a reduction in $CV_{rotation}$ for both $\Phi_{F,687}$ and $\Phi_{F,760}$, with the most substantial improvement seen for G3.

4. Discussion

4.1. Correction of reabsorption and scattering effects at the leaf and canopy

The reabsorption correction method proposed by Gitelson et al. (1998), Van Wittenberghe et al. (2021) and Liu et al. (2020) all utilise the proportional relationship of R_{red} and T_{red} with $f_{esc,687,RS}$ at leaf and canopy level. We compared these methods, and their modifications, with SCOPE simulations of $f_{esc,687}$. Our findings indicate that all proposed models exhibited strong performance in estimating $f_{esc,687,SCOPE}$ for the simulated C_{ab} gradient. However, when applied to measured values, our modifications to the Van Wittenberghe et al. (2021) and Liu et al. (2020) models substantially enhanced the prediction accuracy of $f_{esc,687,SCOPE}$. At leaf level we show that the square root of $f_{esc,687,wit}$ can be used to adjust for the non-linear relationship between R_{red} and T_{red} with $f_{esc,687,SCOPE}$. At canopy level, SCOPE simulations along a *LIA* gradient demonstrated that the estimation of $R_{red,veg}$ is strongly influenced by the *LIA* leading to an increased contribution of $R_{red,soil}$ at high leaf angles. Our results show that for the simulated *LIA* gradient, the approach proposed by Liu et al. (2020) to estimate $R_{red,veg}$ based on

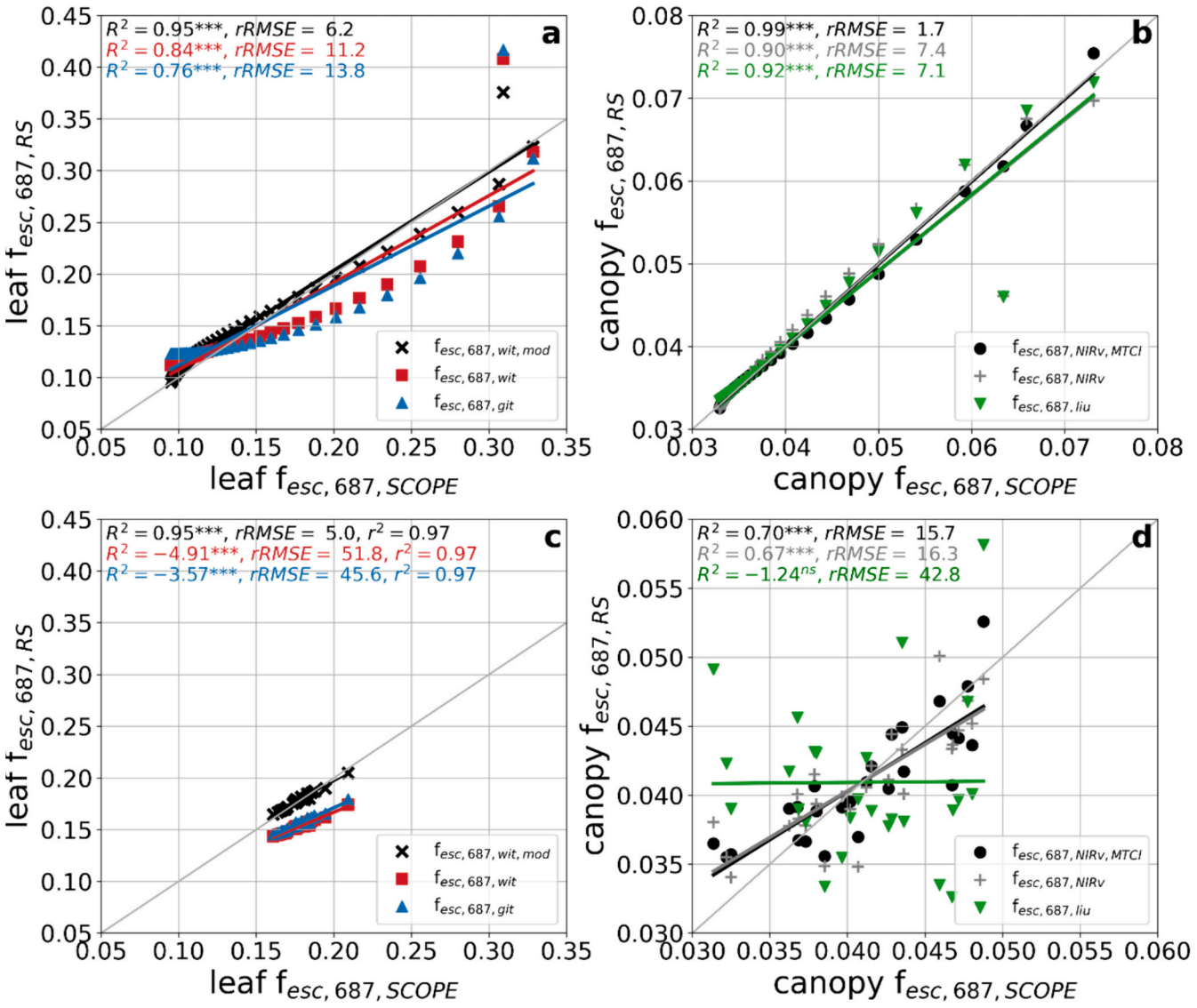

Fig. 7. Comparison between SCOPE-derived and reflectance-based estimates of the leaf (a & c) and canopy (b & d) escape probability of fluorescence at 687 nm ($f_{esc,687}$) using both modelled and observed data. The grey lines represent the 1-to-1 relationship between the SCOPE-derived ($f_{esc,687,SCOPE}$) and reflectance-based ($f_{esc,687,RS}$) estimates of $f_{esc,687}$. Lines represent best fitting linear models. Blue triangles represent estimates of the model proposed by Gitelson et al. (1998), red squares represent estimates of the model proposed by Van Wittenberghe et al. (2021) and black crosses represent the modified Van Wittenberghe et al. (2021) model (a & c). The green triangles in panel b & d represent estimates by the model proposed by Liu et al. (2020), the grey crosses represent estimates by the kNDVI adjusted model of Liu et al. (2020) and the black dots represent estimates by the kNDVI and MTCI adjusted model of Liu et al. (2020). The coefficient of variation (R^2) and the squared Pearson correlation coefficient (r^2) are given with the significance level indicated by the asterisk (ns = P > 0.05, * = P ≤ 0.05, ** = P ≤ 0.01, *** = P ≤ 0.001). The relative root mean square error (rRMSE) is given in percent. The outliers in panel a and b represent values affected by low C_{ab} concentration (<3.5 μg cm-2). (For interpretation of the references to colour in this figure legend, the reader is referred to the web version of this article.)

NDVI results in an overall negative relationship between $R_{red,veg,simulated}$ and $R_{red,veg,VI}$. Given that the potato plants of our experiment exhibited a wide range in *LIA*, were grown in mesocosm filled with bright sandy soil, and lacked understory, it can be explained why the *NDVI* based approach showed low performance when compared to $f_{esc,687,SCOPE}$ (c.f. Fig. 7) and leaf $F_{687,PS}$ (c.f. Fig. 8). It should be noted that the *NDVI*-based estimation of $R_{red,veg}$ showed robust results for the simulated C_{ab} gradient with fixed *LIA*, indicating that *NDVI* may only be a suitable proxy for $R_{red,veg}$ when *LIA* is low and stable. Based on the performance of simulated and retrieved *LIA (c.f.* Fig. 5*)* and C_{ab} gradient (c.f. Fig. 7 & Fig. A.5), we therefore replaced the *NDVI* with NIR_v. Results showed that this modification allowed for an improved prediction of $R_{red,veg}$. SCOPE simulations furthermore showed that under extremely low C_{ab} values (<3.5 μg cm-2), $f_{esc,687}$ decreases, as fluorescence emissions are severely limited by the low amount of chlorophyll. To address this effect, we further introduced *MTCI* which improves the prediction accuracy. We note, however, that our approach needs to be tested for other case-studies, specifically whether the linear scaling of $f_{esc,687}$ changes drastically over different plant individuals, species or functional types.

4.2. Comparability of leaf and canopy fluorescence

When excluding the observed outlier, we found a moderate relationship between leaf and canopy F_{687} and F_{760} (r^2 of 0.3 and 0.34, respectively). After applying the models for $f_{esc,687,wit,mod}$ and $f_{esc,687,NIRv,MTCI}$ the correlation between leaf and canopy $F_{687,PS}$ and $F_{760,PS}$ improved considerably (r^2 of 0.5 and 0.48, respectively). This demonstrates the effectiveness of the two modified correction methods in establishing a more robust association between leaf and canopy fluorescence estimates. The persistent deviation from the 1:1 line in the

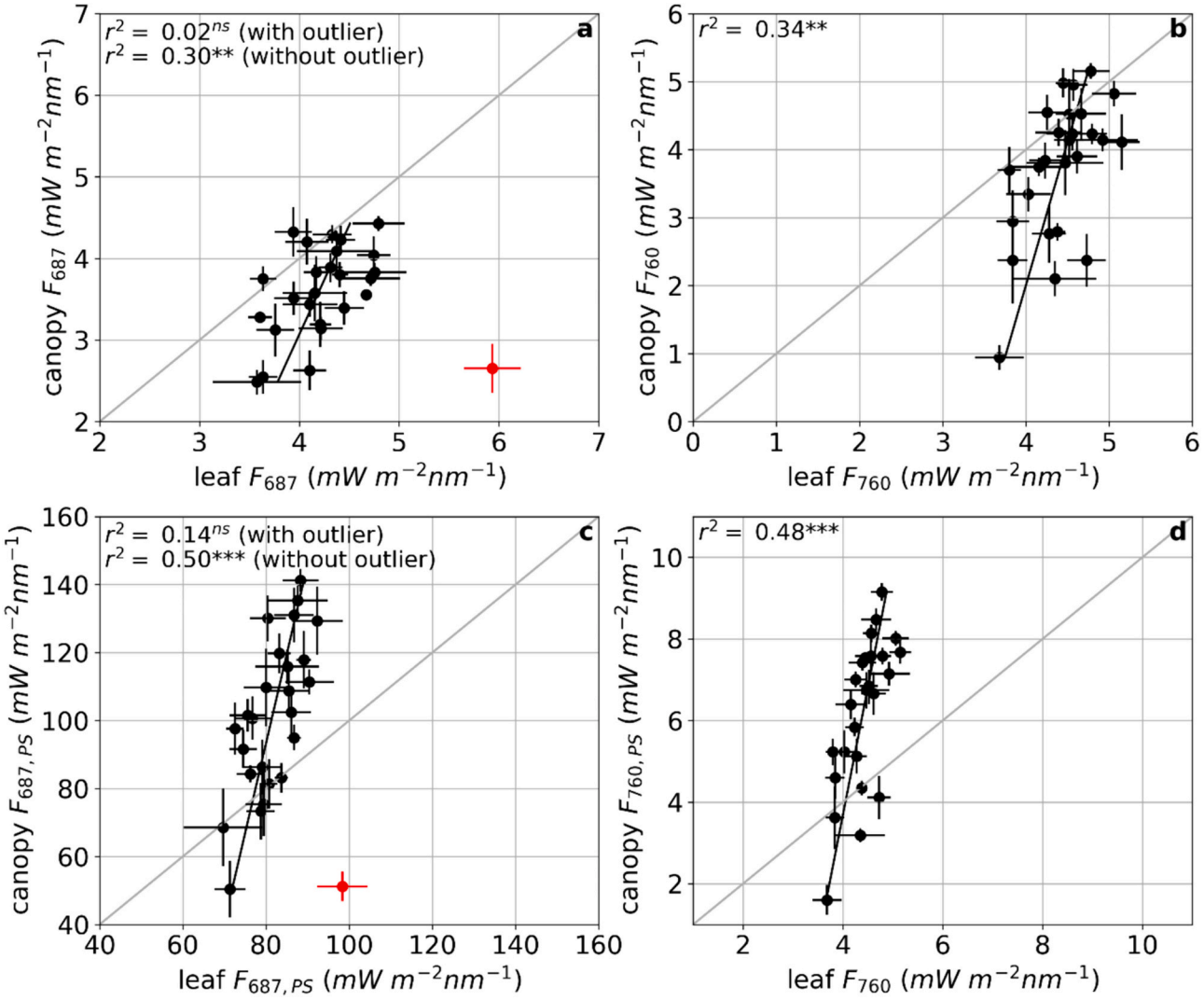

Fig. 8. Relationship between leaf and canopy measured fluorescence at 687 nm (F_{687}) and at 760 nm (F_{760}), as well as fluorescence emitted at the photosystem at 687 nm ($F_{687,PS}$) and at 760 nm ($F_{760,PS}$). Each point represents one mesocosm where 4 leaves and 16 canopy measurements were averaged. The horizontal and vertical lines for each point represent the standard error of the mean. The squared Pearson correlation coefficient (r^2) is given with the significance level indicated by the asterisk (ns = $P > 0.05$, * = $P \leq 0.05$, ** = $P \leq 0.01$, *** = $P \leq 0.001$). The r^2 is given for the best fitting correlation with and without the outlier (red point). The outlier comprises measurements taken on July 24, a day characterised by exceptionally high vapour pressure deficit (>3.3 kPa) and low relative extractable water (<35%). (For interpretation of the references to colour in this figure legend, the reader is referred to the web version of this article.)

corrected values of leaf and canopy $F_{687,PS}$ and $F_{760,PS}$, could be attributed to several factors. First, the leaf and canopy measurements are obtained using different sensors and measurement techniques, which can introduce variations in the data. The FluoWat low pass filter, for instance, cuts the light at 650 nm, resulting in *APAR* values that are up to 20% lower (Van Wittenberghe et al., 2015). Furthermore, we cannot exclude potential artefacts by the approximation of $APAR_{chl}$ by $NDVI_{red}$. Additionally, the physiological and structural differences between individual leaves and the canopy as a whole might also contribute to the differences in fluorescence measurements. Due to the non-linearity of the relationship between Φ_F with Φ_{PQ} and Φ_{NPQ} (Magney et al., 2019; Martini et al., 2022; Wieneke et al., 2022), measurements conducted under low light conditions (<400 mmol m-^{2} s-1) or when the plant is affected by severe stress (photoinhibition), can be mis $CV_{rotation}$ preted. In this study, measurements were conducted between 800 and 1200 mmol m^{-2} s^{-1} PAR and therefore no measurement under low sunlight conditions could have occurred at the leaf level. However, leaves within the canopy were partially shaded, which was not the case for measured leaves. As shaded leaves contributed to the overall canopy signal, the responses of F_{687} and F_{760} to stress may have been attenuated at the canopy level (Liu et al., 2019a). This suggests that some of the individual leaves might have been more affected by heat and drought stress than the simultaneously measured canopy. This could also explain the observed outlier in Fig. 8, where the lowest values of F_{687} and $F_{687,PS}$ were measured for the canopy and highest values at the leaf. The combination of high light intensity, low soil water availability, and high vapour pressure deficit conditions could have potentially induced an upregulation in Φ_F for these leaf measurements under severe drought stress. In general, we did not observe any increase in canopy-level Φ_F, suggesting that the canopy signal was not as strongly affected by heat and drought stress as the individual leaves might have been. Despite the application of correction methods, these inherent differences and sources of variability can therefore limit the strength of the relationship between leaf and canopy fluorescence measurements. These results stress the complexity of obtaining foliar samples that are representative of the plant physiological status.

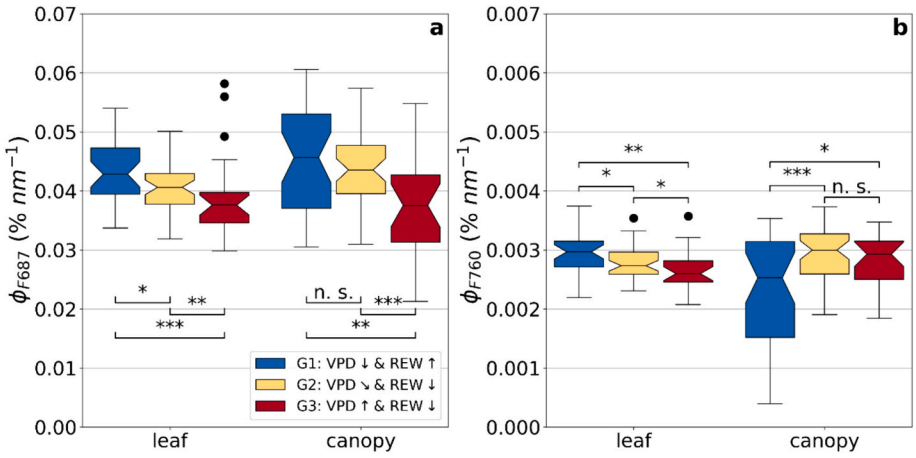

Fig. 9. Box plots showing the distribution of the quantum yield of fluorescence at 687 nm ($\Phi_{F,687}$) and at 760 nm ($\Phi_{F,760}$) within each stress group. Group one (G1) comprises measurements influenced by concurrent moderate REW (≥0.4) and low VPD (≤1.4 hPa), as well as concurrent high REW (≥0.6) and high VPD (≤2.5 hPa). Group three (G3) includes measurements affected by simultaneous high VPD (≥1.4 hPa) and low REW (≤0.15), as well as very high VPD (≤3.0 hPa) and high REW (≥0.75). Group two (G2) encompasses measurements not categorised in G1 and G3. The significant difference between each group are shown by the asterisk (ns = $P > 0.05$, * = $P \leq 0.05$, ** = $P \leq 0.01$, *** = $P \leq 0.001$) above the box plots and were calculated by applying the Kruskal-Wallis significance test. The vertical line within the box plots represents the medians, the lower whiskers represent the first quartile, the upper whisker the third quartile, the black dots represent the outliers.

4.3. Leaf and canopy $\Phi_{F,687}$ and $\Phi_{F,760}$ under increasing drought and heat stress

As previously discussed, Φ_F, Φ_{PQ}, and Φ_{NPQ} exhibit a nonlinear relationship that is primarily influenced by environmental stress (Magney et al., 2019; Martini et al., 2022; Mohammed et al., 2019; van der Tol et al., 2014; Wieneke et al., 2022). When light availability is limited and becomes a constraint for photosynthesis, Φ_F and Φ_{NPQ} values tend to be relatively low, while Φ_{PQ} is high (e.g., during the early morning hours). As light intensity increases, and moderate stress emerges (e.g., over the morning hours), Φ_{PQ} decrease while Φ_{NPQ} and Φ_F increase. With increasing air temperature, decreasing water availability, or nutrient limitations, excessive light energy is dissipated primarily through non-photochemical quenching. As a result, Φ_{NPQ} increases while both Φ_F and Φ_{PQ} decrease. In such situations, Φ_F and Φ_{PQ} exhibit a positive linear relationship, indicating that the reduction in Φ_F is accompanied by a corresponding decrease in Φ_{PQ}. Under intense light and severe environmental stress (photoinhibition) Φ_F might increase while Φ_{PQ} further decreases (Magney et al., 2019; Martini et al., 2022; Wieneke et al., 2022). This complex relationship reflects the dynamic balance between energy dissipation and utilisation in response to stressors. In our study, we found a consistent decrease in leaf and canopy $\Phi_{F,687}$, as well as leaf $\Phi_{F,760}$, with increasing drought and heat stress, as shown in Fig. 9. We assume that photoinhibition, a process associated with the impairment of photosynthetic efficiency under high light and stress conditions, might have been only observed in one specific mesocosm measurement at the end of the campaign. This particular mesocosm exhibited high temperatures of 38 °C and a low volumetric soil water content of under 5% (REW < 35%), leading to an increase of leaf $\Phi_{F,687}$ and $\Phi_{F,760}$, as indicated by the high-value outliers in Fig. 9.

Interestingly, we observed a deviating pattern in canopy $\Phi_{F,760}$ compared to leaf and canopy $\Phi_{F,687}$ and leaf $\Phi_{F,760}$ (leaf and canopy $\Phi_{F,687}$, as well as leaf $\Phi_{F,760}$). The canopy $\Phi_{F,760}$ values G1 showed a strong variance and appeared to be consistently lower than that of G2 and G3. This discrepancy suggests that there might be additional factors at play, specifically affecting the interpretation of fluorescence efficiency in the far-red region at canopy level. In section 3.3, we examined whether the SVD retrieval method yields distinct patterns in leaf and canopy $\Phi_{F,687}$ and $\Phi_{F,760}$. However, we found that a very similar pattern persisted compared to the SFM retrieval method. We therefore exclude that the distinct pattern in canopy $\Phi_{F,760}$ is caused by a retrieval artefact in the SFM method.

Other relevant factors might include variations in light penetration or solar incident angle which could result in a higher variability in canopy $\Phi_{F,760}$. Our mesocosm rotation experiment showed that the CV was more pronounced for the far-red efficiency values than for the red, particularly evident in G1 and G2. Even though the correction methods reduced $CV_{rotation}$ for red and far-red Φ_F, the CV remained high for $\Phi_{F,760}$. The hypothesis of a generally higher variation in $\Phi_{F,760}$ as an explanation for the higher CV in $\Phi_{F,760}$ compared to $\Phi_{F,687}$ can be dismissed, since Fig. 9 illustrates that canopy values of $\Phi_{F,687}$ and $\Phi_{F,760}$ exhibit a very similar spread. Since $CV_{rotation}$ of $\Phi_{F,687}$ was less affected by changing solar incidence angle compared to that of $\Phi_{F,760}$, it suggests that canopy scattering effects and soil reflectance might not fully corrected by f_{esc}, on which the estimation of $\Phi_{F,760}$ relies on. This finding is highly relevant, as $\Phi_{F,760}$ is commonly regarded as a more reliable fluorescence signal due to its lower retrieval uncertainty (e.g., Cendrero-Mateo et al. (2019).

4.4. Implications of our findings for satellite-derived sun-induced fluorescence

Our findings emphasise the importance of exercising caution when using $\Phi_{F,760}$ as the sole indicator of photosynthetic efficiency. Further investigation on whether the limitations discussed here are specific to certain measurement configurations or reflect broader insufficiencies in the current correction methods is needed. It is worth noting that satellite-derived SIF integrates signals over larger spatial scales, which may mitigate some of the issues observed at the leaf and canopy levels. Nevertheless, we recommend conducting careful testing to assess the validity and robustness of current correction methods, considering the potential implications for accurate estimation of photosynthetic efficiency using $\Phi_{F,760}$. Our study also revealed that reabsorption-corrected $F_{687,PS}$ holds great potential for tracking drought and heat stress, as it exhibits a stronger relationship with PSII and the downregulation of photosynthesis under stress compared to $F_{760,PS}$ (Xu et al., 2021). Additionally, $F_{687,PS}$ was found to be less influenced by changes in the solar incidence angle, further supporting its robustness as an indicator of plant stress.

These findings highlight the advantages of $F_{687,PS}$ in monitoring and assessing plant responses to environmental stressors, particularly in the context of drought and heat stress. To validate and generalise the effectiveness of the here proposed correction method for red fluorescence, it is important to test it across a wider range of plant species.

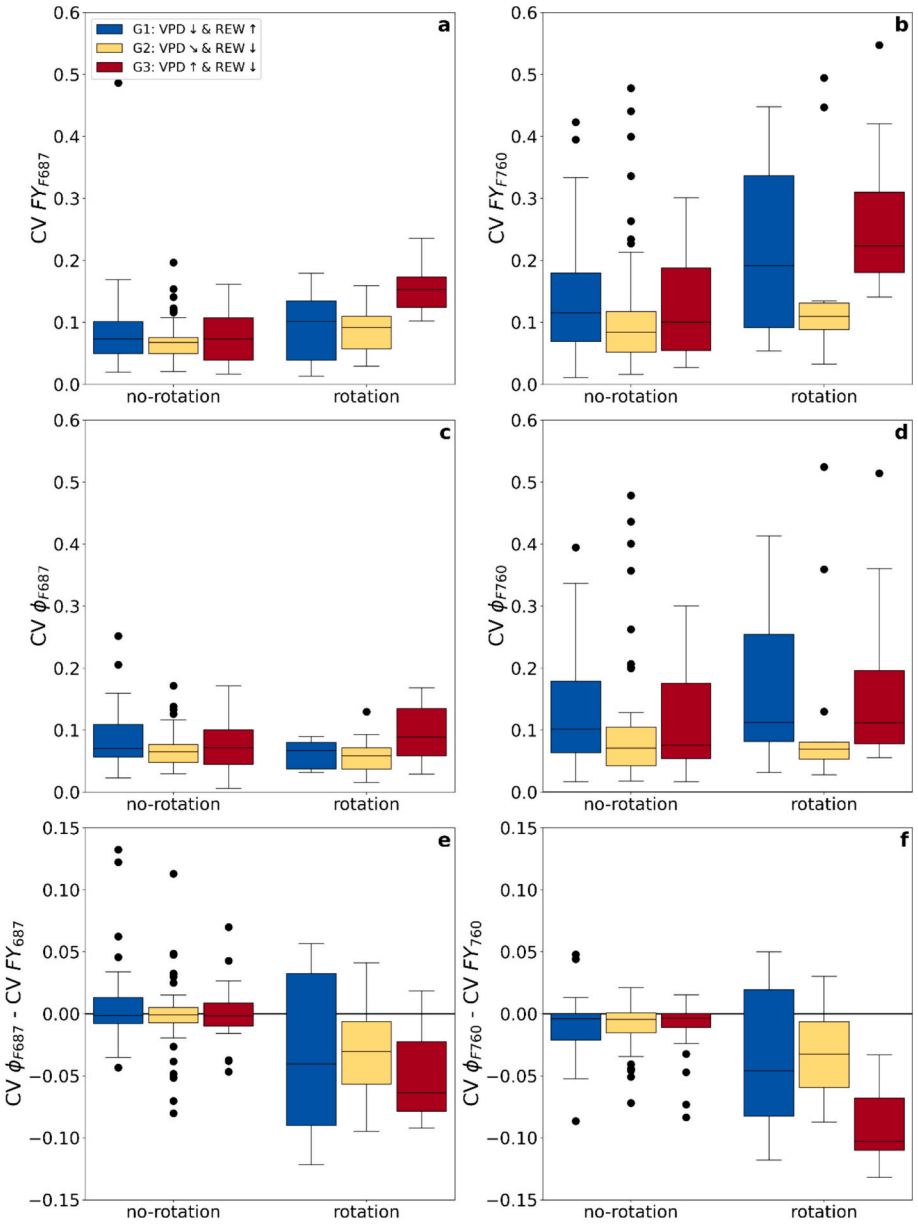

Fig. 10. Box plots in panel a and b showing the distribution of the coefficient of variation for canopy derived fluorescence yield at 687 nm (CV FY_{687}) and at 760 nm (CV FY_{760}) within each stress group, respectively. Panel c and d showing the distribution of the coefficient of variation for canopy derived quantum yield of fluorescence at 687 nm (CV $\Phi_{F,687}$) and at 760 nm (CV $\Phi_{F,760}$) within each stress group, respectively. Panel e and f show the difference between CV $\Phi_{F,687}$ and CV FY_{687} as well as the difference between CV $\Phi_{F,760}$ and CV FY_{760}, respectively. Negative values indicate a reduction and positive values an increase in the CV after applying the corresponding f_{esc} factor Group one (G1) comprises measurements influenced by concurrent moderate REW ($\geq$0.4) and low VPD ($\leq$1.4 hPa), as well as concurrent high REW ($\geq$0.6) and high VPD ($\leq$2.5 hPa). Group three (G3) includes measurements affected by simultaneous high VPD ($\geq$1.4 hPa) and low REW ($\leq$0.15), as well as very high VPD ($\leq$3.0 hPa) and high REW ($\geq$0.75). Group two (G2) encompasses measurements not categorised in G1 and G3. The significant difference between each group are shown by the asterisk (ns = $P > 0.05$, * = $P \leq 0.05$, ** = $P \leq 0.01$) above the box plots and were calculated by applying the Kruskal-Wallis significance test. The vertical line within the box plots represents the medians, the lower whiskers represent the first quartile, the upper whisker the third quartile, the black dots represent the outliers.

Different plant species and soil backgrounds may exhibit variations in their spectral properties, physiological responses, and structural characteristics, which can impact the accuracy and generality of reabsorption and scattering correction methods.

5. Conclusion

This study aimed to explore the relationship between leaf and canopy-level fluorescence measurements under increasing heat and drought stress conditions and to determine their potential as reliable indicators of plant stress. To accomplish this goal, we evaluated existing correction methods for red and far-red fluorescence and proposed modifications to the red fluorescence methods to enhance the prediction of $f_{esc,687}$ at both leaf and canopy levels. Our proposed model adjustments, along with the correction method for far-red fluorescence by Zeng et al. (2019), proved effective in enhancing the consistency between leaf and canopy-level measurements. This finding highlights the importance of appropriate correction methods in establishing accurate relationships between leaf and canopy measurements. However, the interpretation of $\Phi_{F,760}$, despite the improvement provided by the correction, proved to be challenging probably due to structural effects that were not fully accounted for by the existing correction methods.

This discrepancy warrants further investigation to better understand and address the limitations in correcting $\Phi_{F,760}$ caused by structural effects. On the other hand, $\Phi_{F,687}$ demonstrated its potential as an indicator for assessing plant responses to drought and heat stress.

In light of these findings, we recommend conducting further research to investigate the specific causes of possible discrepancies between leaf and canopy measurements of $\Phi_{F,760}$. Additionally, exploring the ability of $\Phi_{F,687}$ to detect plant stress and monitor photosynthetic down-regulation in a broader range of plant species and stress conditions would provide valuable insights for practical applications and enhance our understanding of plant responses to environmental stressors.

Declaration of AI and AI-assisted technologies in the writing process

During the preparation of this work the authors used ChatGPT in order to improve readability and language. After using ChatGPT, the authors reviewed and edited the content as needed and take full responsibility for the content of the publication.

CRediT authorship contribution statement

Sebastian Wieneke: Writing – review & editing, Writing – original draft, Visualization, Validation, Methodology, Investigation, Funding acquisition, Formal analysis, Data curation, Conceptualization. **Javier Pacheco-Labrador:** Writing – review & editing, Writing – original draft, Software, Methodology, Formal analysis, Conceptualization. **Miguel D. Mahecha:** Writing – review & editing, Writing – original draft, Supervision, Funding acquisition. **Sílvia Poblador:** Writing – original draft, Investigation, Conceptualization. **Sara Vicca:** Writing – review & editing, Writing – original draft, Supervision, Conceptualization. **Ivan A. Janssens:** Writing – review & editing, Writing – original draft, Supervision, Resources, Conceptualization.

Declaration of competing interest

Sebastian Wieneke reports financial support was provided by European Union.

Data availability

Data will be made available on request.

Acknowledgements

This research was supported by the Research Foundation— Flanders (FWO), and by The Research Council of the University of Antwerp. Sebastian Wieneke has received funding from the European Union Horizon 2020 Research and Innovation program under the Marie Skłodowska-Curie grant (ReSPEc, grant no 795299). Sílvia Poblador was financially supported by a Postdoctoral Marie Skłodowska-Curie actions - Seal of Excellence Fellowship of the Research Foundation – Flanders (MSCA SoE FWO, 12ZZ521N).

Appendix A

Fig. A.1. Pictures of the experimental setup. The study site was located at the Experimental site on the Drie Eiken Campus of the University of Antwerp in Belgium, situated at 51°09′ N, 04°24′ E. The experiment consists of ten mesocosms with five control and five drought treatments. The mesocosms were placed on movable plates to allow for unobstructed clear sky measurements outside of the shelter.

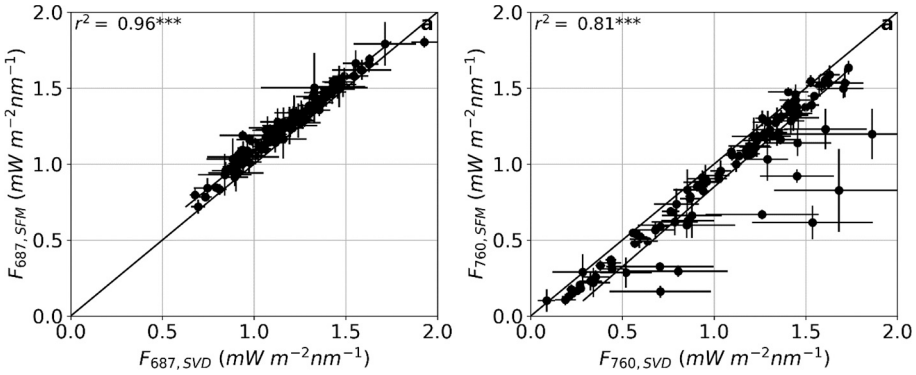

Fig. A.2. Correlation between SFM and SVD retrieved red and far-red fluorescence. Each point represents the mean of 4 canopy measurements. The horizontal and vertical lines for each point represent the standard error of the mean. The squared Pearson correlation coefficient (r^2) is given with the significance level indicated by the asterisk (*** = $P \leq 0.001$). (For interpretation of the references to colour in this figure legend, the reader is referred to the web version of this article.)

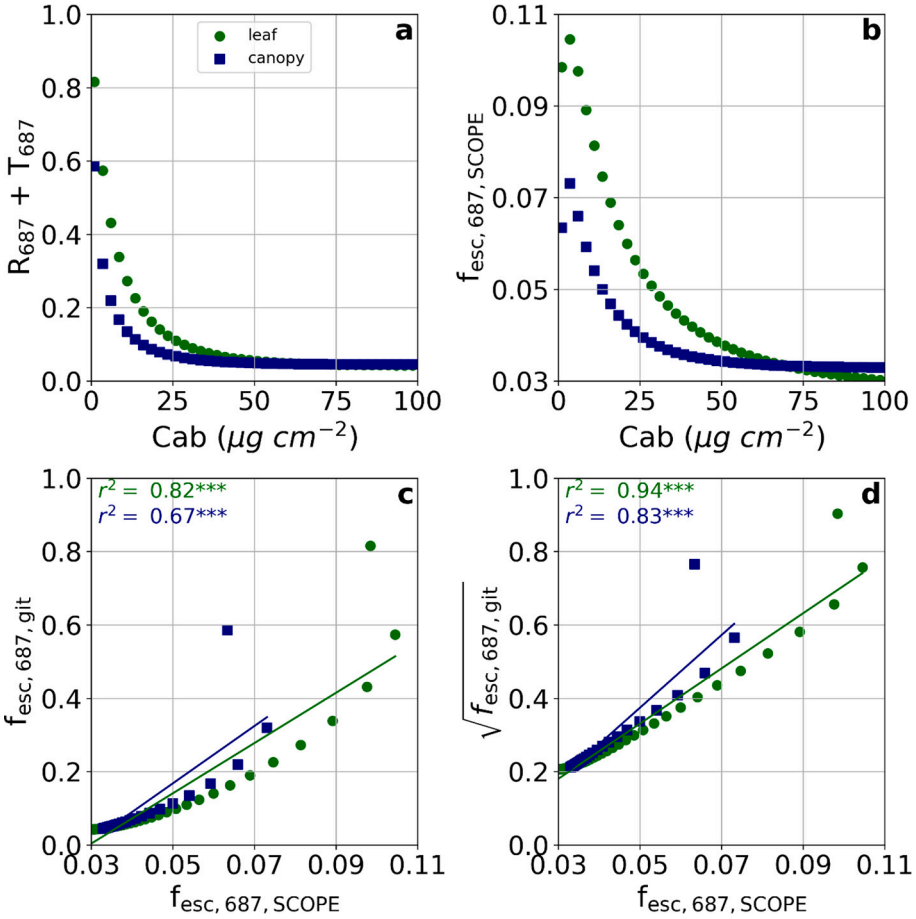

Fig. A.3. a) relationship of leaf (green circles) and canopy (blue squares) reflectance at 687 nm (R_{687}) and the chlorophyll a&b (Cab) concentration. b) relationship of leaf and canopy escape probability of sun-induced fluorescence at 687 nm estimated from the radiative transfer model SCOPE ($f_{esc,687,SCOPE}$) and Cab concentration. c) relationship of estimated $f_{esc,687}$ derived from Gitelson et al. (1998) ($f_{esc,687,git}$) and $f_{esc,687,SCOPE}$. d) relationship of estimated $f_{esc,687}$ derived from modified version of Gitelson et al. (1998) ($f_{esc,687,git,mod}$) and $f_{esc,687,SCOPE}$. The squared Pearson correlation coefficient (r^2) is given with the significance level indicated by the asterisk (*** = $P \leq 0.001$).

Table A.1
Equations and model fitting parameters for the used $f_{esc,687}$ models.

Leaf models:	a	b
$f_{esc,687,git} \approx (R_{687} + T_{687}) \bullet a + b$	0.40	0.106
	0.74	0.106
$f_{esc,687,wit} \approx \left(\frac{F_{up687} + F_{dw,687}}{\frac{F_{up,687}}{R_{687}} + \frac{F_{dw,687}}{T_{687}}} \right) \bullet a + b$		

(*continued on next page*)

Table A.1 (*continued*)

Leaf models:	a	b
$f_{esc,687,wit,mod} \approx \left(\sqrt{\frac{F_{up687} + F_{dw,687}}{\frac{F_{up,687}}{R_{687}} + \frac{F_{dw,687}}{T_{687}}}} \right) \bullet a + b$	0.51	0.05
Canopy models:	a	b
$f_{esc,687,Liu} \sim \left(\frac{R_{red,total} \bullet NDVI^2}{fAPAR_{green}} \right) \bullet a + b$	0.778	0.0084
$f_{esc,687,NIRv} \sim \left(\frac{R_{red,total} \bullet {NIR_v}^2}{fAPAR_{green}} \right) \bullet a + b$	2.565	0.0095
$f_{esc,687,kNDVI,NIRv} \sim \left(\frac{R_{red,total} \bullet {NIR_v}^2}{fAPAR_{green} \bullet \sqrt{MTCI}} \right) \bullet a + b$	2.480	0.0173

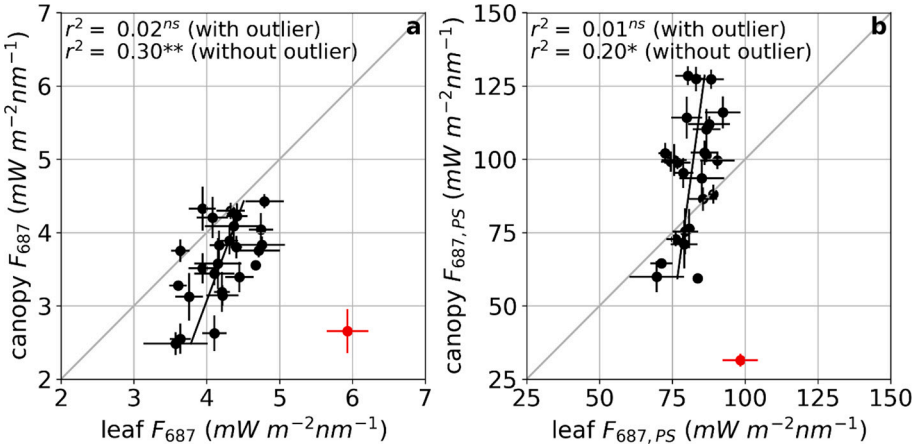

Fig. A.4. Relationship between leaf and canopy measured fluorescence at 687 nm (a; F_{687}) and fluorescence emitted at the photosystem at 687 nm (b; $F_{687,PS}$). $F_{687,PS}$ was calculated based on Liu et al. (2020). Each point represents one mesocosm where 4 leaves and 16 canopy measurements were averaged. The horizontal and vertical lines for each point represent the standard error of the mean. The squared Pearson correlation coefficient (r^2) is given with the significance level indicated by the asterisk (ns = P > 0.05, * = P ≤ 0.05, ** = P ≤ 0.01, *** = P ≤ 0.001). The r^2 is given for the best fitting correlation with and without the outlier (red point). The outlier comprises measurements taken on July 24, a day characterised by exceptionally high vapour pressure deficit (>3.3 kPa) and low relative extractable water (<35%). (For interpretation of the references to colour in this figure legend, the reader is referred to the web version of this article.)

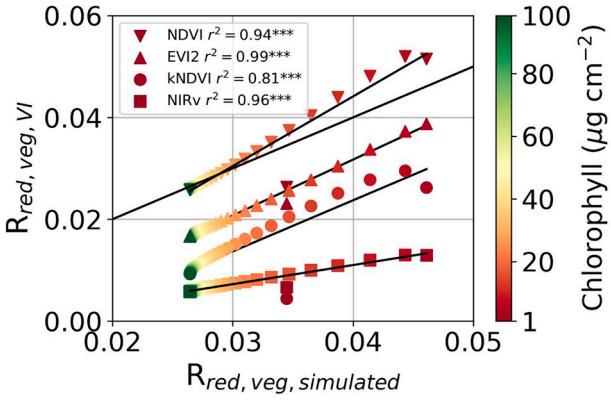

Fig. A.5. Relationship between $R_{red,veg}$ derived from vegetation indices ($R_{red,veg,VI}$) and $R_{red,veg}$ derived from SCOPE ($R_{red,veg,simulated}$) under a chlorophyll gradient. Inverted Pyramid symbols represent the NDVI (normalized difference vegetation index), pyramid symbols represent the EVI2 (enhanced vegetation index 2), circle symbols represent the kNDVI (kernel NDVI) and square symbols represent the NIRv (near infrared of vegetation) The squared Pearson correlation coefficient (r^2) is given with the significance level indicated by the asterisk (ns = P > 0.05, * = P ≤ 0.05, ** = P ≤ 0.01, *** = P ≤ 0.001).

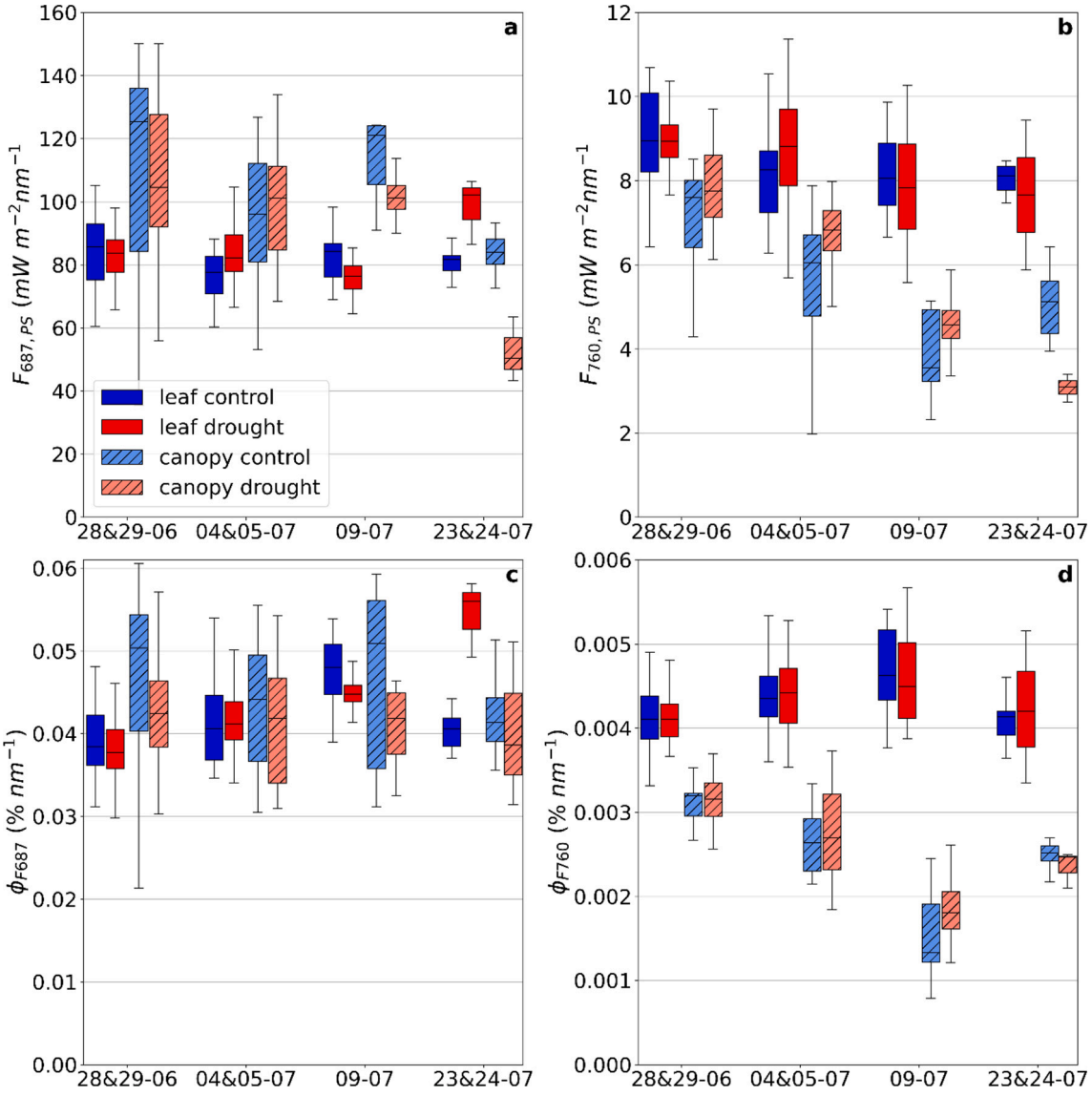

Fig. A.6. Box plots showing the distribution of red (a) and far-red (b) sun induced fluorescence emitted at the PS ($F_{687,PS}$ & $F_{760,PS}$) and the quantum yield of fluorescence at 687 nm (c; $\Phi_{F,687}$) and at 760 nm (d; $\Phi_{F,760}$) throughout the measurement campaign. The blue boxes represent the spread within the five control mesocosms, the red boxes represent the spread within the five drought mesocosms. All mesocosm where placed under a transparent shelter to exclude natural wetting. The control mesocosm were regularly watered with tap water. Non-hatched boxes indicate leaf-level measurements, while hatched boxes indicate canopy-level measurements. (For interpretation of the references to colour in this figure legend, the reader is referred to the web version of this article.)

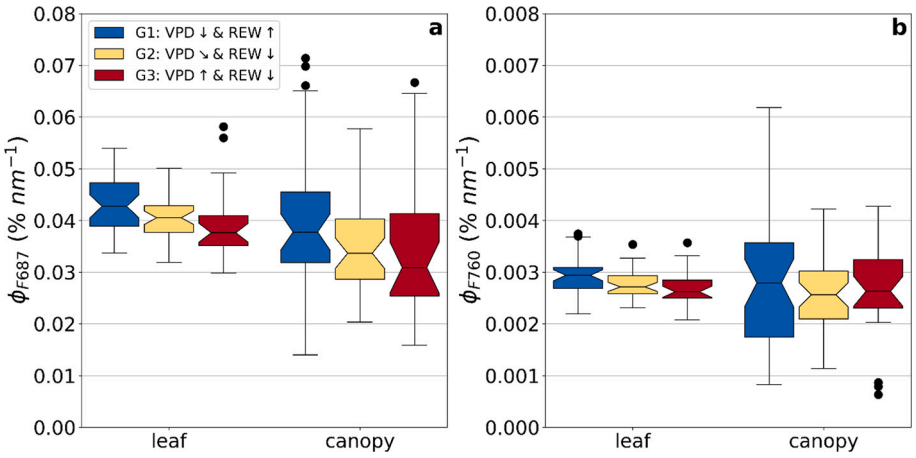

Fig. A.7. Box plots showing the distribution of the quantum yield of fluorescence at 687 nm ($\Phi_{F,687}$) and at 760 nm ($\Phi_{F,760}$) within each stress group and derived from the singular value decomposition (SVD) retrieval method. Group one (G1) comprises measurements influenced by concurrent moderate REW (≥0.4) and low VPD (≤1.4 hPa), as well as concurrent high REW (≥0.6) and high VPD (≤2.5 hPa). Group three (G3) includes measurements affected by simultaneous high VPD (≥1.4 hPa) and low REW (≤0.15), as well as very high VPD (≤3.0 hPa) and high REW (≥0.75). Group two (G2) encompasses measurements not categorised in G1 and G3. The significant difference between each group are shown by the asterisk (ns = P > 0.05, * = P ≤ 0.05, ** = P ≤ 0.01, *** = P ≤ 0.001) above the box plots and were calculated by applying the Kruskal-Wallis significance test. The vertical line within the box plots represents the medians, the lower whiskers represent the first quartile, the upper whisker the third quartile, the black dots represent the outliers.

References

Ač, A., Malenovský, Z., Olejníčková, J., Gallé, A., Rascher, U., Mohammed, G., 2015. Meta-analysis assessing potential of steady-state chlorophyll fluorescence for remote sensing detection of plant water, temperature and nitrogen stress. Remote Sens. Environ. 168, 420–436. https://doi.org/10.1016/j.rse.2015.07.022.

Barrs, H., Weatherley, P., 1962. A re-examination of the relative turgidity technique for estimating water deficits in leaves. Aust. Jnl. Of Bio. Sci. 15, 413. https://doi.org/10.1071/BI9620413.

Bartlett, M.K., Scoffoni, C., Sack, L., 2012. The determinants of leaf turgor loss point and prediction of drought tolerance of species and biomes: a global meta-analysis. Ecol. Lett. 15, 393–405. https://doi.org/10.1111/j.1461-0248.2012.01751.x.

Bousquet, L., Lachérade, S., Jacquemoud, S., Moya, I., 2005. Leaf BRDF measurements and model for specular and diffuse components differentiation. Remote Sens. Environ. 98, 201–211. https://doi.org/10.1016/j.rse.2005.07.005.

Buschmann, C., 2007. Variability and application of the chlorophyll fluorescence emission ratio red/far-red of leaves. Photosynth. Res. 92, 261–271. https://doi.org/10.1007/s11120-007-9187-8.

Butler, W.L., 1978. Energy distribution in the photochemical apparatus of photosynthesis. Annu. Rev. Plant Physiol. 29, 345–378. https://doi.org/10.1146/annurev.pp.29.060178.002021.

Camps-Valls, G., Campos-Taberner, M., Moreno-Martínez, Á., Walther, S., Duveiller, G., Cescatti, A., Mahecha, M.D., Muñoz-Marí, J., García-Haro, F.J., Guanter, L., Jung, M., Gamon, J.A., Reichstein, M., Running, S.W., 2021. A unified vegetation index for quantifying the terrestrial biosphere. Sci. Adv. 7, eabc7447. https://doi.org/10.1126/sciadv.abc7447.

Celesti, M., van der Tol, C., Cogliati, S., Panigada, C., Yang, P., Pinto, F., Rascher, U., Miglietta, F., Colombo, R., Rossini, M., 2018. Exploring the physiological information of Sun-induced chlorophyll fluorescence through radiative transfer model inversion. Remote Sens. Environ. 215, 97–108. https://doi.org/10.1016/j.rse.2018.05.013.

Cendrero-Mateo, M.P., Wieneke, S., Damm, A., Alonso, L., Pinto, F., Moreno, J., Guanter, L., Celesti, M., Rossini, M., Sabater, N., Cogliati, S., Julitta, T., Rascher, U., Goulas, Y., Aasen, H., Pacheco-Labrador, J., Mac Arthur, A., 2019. Sun-induced chlorophyll fluorescence III: benchmarking retrieval methods and sensor characteristics for proximal sensing. Remote Sens. 11, 962. https://doi.org/10.3390/rs11080962.

Chang, C.Y., Guanter, L., Frankenberg, C., Köhler, P., Gu, L., Magney, T.S., Grossmann, K., Sun, Y., 2020. Systematic assessment of retrieval methods for canopy far-red solar-induced chlorophyll fluorescence using high-frequency automated field spectroscopy. J. Geophys. Res. Biogeosci. 125 https://doi.org/10.1029/2019JG005533 e2019JG005533.

Cogliati, S., Verhoef, W., Kraft, S., Sabater, N., Alonso, L., Vicent, J., Moreno, J., Drusch, M., Colombo, R., 2015. Retrieval of sun-induced fluorescence using advanced spectral fitting methods. Remote Sens. Environ. 169, 344–357. https://doi.org/10.1016/j.rse.2015.08.022.

Damm, A., Erler, A., Hillen, W., Meroni, M., Schaepman, M.E., Verhoef, W., Rascher, U., 2011. Modeling the impact of spectral sensor configurations on the FLD retrieval accuracy of sun-induced chlorophyll fluorescence. Remote Sens. Environ. 115, 1882–1892. https://doi.org/10.1016/j.rse.2011.03.011.

Dash, J., Curran, P.J., 2004. The MERIS terrestrial chlorophyll index. Int. J. Remote Sens. 25, 5403–5413. https://doi.org/10.1080/01431160420002740l5.

Dash, J., Curran, P.J., 2007. Evaluation of the MERIS terrestrial chlorophyll index (MTCI). Advances in Space Research 39, 100–104. https://doi.org/10.1016/j.asr.2006.02.034.

Dechant, B., Ryu, Y., Badgley, G., Zeng, Y., Berry, J.A., Zhang, Y., Goulas, Y., Li, Z., Zhang, Q., Kang, M., Li, J., Moya, I., 2020. Canopy structure explains the relationship between photosynthesis and sun-induced chlorophyll fluorescence in crops. Remote Sens. Environ. 241, 111733 https://doi.org/10.1016/j.rse.2020.111733.

Gamon, J.A., Serrano, L., Surfus, J.S., 1997. The photochemical reflectance index: an optical indicator of photosynthetic radiation use efficiency across species, functional types, and nutrient levels. Oecologia 112, 492–501. https://doi.org/10.1007/s004420050337.

Gitelson, A.A., Buschmann, C., Lichtenthaler, H.K., 1998. Leaf chlorophyll fluorescence corrected for re-absorption by means of absorption and reflectance measurements. J. Plant Physiol. 152, 283–296. https://doi.org/10.1016/S0176-1617(98)80143-0.

Guanter, L., Rossini, Micol, Colombo, R., Meroni, M., Frankenberg, C., Lee, J.-E., Joiner, J., 2013. Using field spectroscopy to assess the potential of statistical approaches for the retrieval of sun-induced chlorophyll fluorescence from ground and space. Remote Sens. Environ. 133, 52–61. https://doi.org/10.1016/j.rse.2013.01.017.

Guanter, L., Zhang, Y., Jung, M., Joiner, J., Voigt, M., Berry, J.A., Frankenberg, C., Huete, A.R., Zarco-Tejada, P., Lee, J.-E., Moran, M.S., Ponce-Campos, G., Beer, C., Camps-Valls, G., Buchmann, N., Gianelle, D., Klumpp, K., Cescatti, A., Baker, J.M., Griffis, T.J., 2014. Global and time-resolved monitoring of crop photosynthesis with chlorophyll fluorescence. PNAS 111, E1327–E1333. https://doi.org/10.1073/pnas.1320008111.

Hwang, Y., Kim, J., Ryu, Y., 2023. Canopy structural changes explain reductions in canopy-level solar induced chlorophyll fluorescence in Prunus yedoensis seedlings under a drought stress condition. Remote Sens. Environ. 296, 113733 https://doi.org/10.1016/j.rse.2023.113733.

Jiang, Z., Huete, A.R., Didan, K., Miura, T., 2008. Development of a two-band enhanced vegetation index without a blue band. Remote Sens. Environ. 112, 3833–3845. https://doi.org/10.1016/j.rse.2008.06.006.

Joiner, J., Yoshida, Y., Guanter, L., Middleton, E.M., 2016. New methods for the retrieval of chlorophyll red fluorescence from hyperspectral satellite instruments: simulations and application to GOME-2 and SCIAMACHY. Atmos. Meas. Tech. 9, 3939–3967. https://doi.org/10.5194/amt-9-3939-2016.

Jonard, F., De Cannière, S., Brüggemann, N., Gentine, P., Short Gianotti, D.J., Lobet, G., Miralles, D.G., Montzka, C., Pagán, B.R., Rascher, U., Vereecken, H., 2020. Value of sun-induced chlorophyll fluorescence for quantifying hydrological states and fluxes: current status and challenges. Agric. For. Meteorol. 291, 108088 https://doi.org/10.1016/j.agrformet.2020.108088.

Julitta, T., 2017. FieldSpectroscopy CC and FieldSpectroscopy DP Packages.

Julitta, T., Wutzler, T., Rossini, M., Colombo, R., Cogliati, S., Meroni, M., Burkart, A., 2017. An R Package for Field Spectroscopy: From System Characterization to Sun-Induced Chlorophyll Fluorescence Retrieval.

Kim, J., Ryu, Y., Dechant, B., Lee, H., Kim, H.S., Kornfeld, A., Berry, J.A., 2021. Solar-induced chlorophyll fluorescence is non-linearly related to canopy photosynthesis in a temperate evergreen needleleaf forest during the fall transition. Remote Sens. Environ. 258, 112362 https://doi.org/10.1016/j.rse.2021.112362.

Köhler, P., Behrenfeld, M.J., Landgraf, J., Joiner, J., Magney, T.S., Frankenberg, C., 2020. Global retrievals of solar-induced chlorophyll fluorescence at red wavelengths

with TROPOMI. Geophys. Res. Lett. 47, e87541 https://doi.org/10.1029/2020GL087541.
Kreith, F., Kreider, J.F., 1978. Principles of Solar Engineering. Hemisphere Publishing Corporation.
Lichtenthaler, H.K., Rinderle, U., 1988. The role of chlorophyll fluorescence in the detection of stress conditions in plants. C R C Crit. Rev. Anal. Chem. 19, S29–S85. https://doi.org/10.1080/15476510.1988.10401466.
Liu, W., Atherton, J., Mõttus, M., Gastellu-Etchegorry, J.-P., Malenovský, Z., Raumonen, P., Åkerblom, M., Mäkipää, R., Porcar-Castell, A., 2019a. Simulating solar-induced chlorophyll fluorescence in a boreal forest stand reconstructed from terrestrial laser scanning measurements. Remote Sens. Environ. 232, 111274 https://doi.org/10.1016/j.rse.2019.111274.
Liu, X., Guanter, L., Liu, L., Damm, A., Malenovský, Z., Rascher, U., Peng, D., Du, S., Gastellu-Etchegorry, J.-P., 2019b. Downscaling of solar-induced chlorophyll fluorescence from canopy level to photosystem level using a random forest model. Remote Sens. Environ. 231, 110772 https://doi.org/10.1016/j.rse.2018.05.035.
Liu, X., Liu, L., Hu, J., Guo, J., Du, S., 2020. Improving the potential of red SIF for estimating GPP by downscaling from the canopy level to the photosystem level. Agric. For. Meteorol. 281, 107846 https://doi.org/10.1016/j.agrformet.2019.107846.
Liu, Y., Chen, J.M., He, L., Zhang, Z., Wang, R., Rogers, C., Fan, W., de Oliveira, G., Xie, X., 2022. Non-linearity between gross primary productivity and far-red solar-induced chlorophyll fluorescence emitted from canopies of major biomes. Remote Sens. Environ. 271, 112896 https://doi.org/10.1016/j.rse.2022.112896.
López, J., Way, D.A., Sadok, W., 2021. Systemic effects of rising atmospheric vapor pressure deficit on plant physiology and productivity. Glob. Chang. Biol. 27, 1704–1720. https://doi.org/10.1111/gcb.15548.
Magney, T.S., Frankenberg, C., Köhler, P., North, G., Davis, T.S., Dold, C., Dutta, D., Fisher, J.B., Grossmann, K., Harrington, A., Hatfield, J., Stutz, J., Sun, Y., Porcar-Castell, A., 2019. Disentangling changes in the spectral shape of chlorophyll fluorescence: implications for remote sensing of photosynthesis. J. Geophys. Res. Biogeosci. 124, 1491–1507. https://doi.org/10.1029/2019JG005029.
Martini, D., Sakowska, K., Wohlfahrt, G., Pacheco-Labrador, J., van der Tol, C., Porcar-Castell, A., Magney, T.S., Carrara, A., Colombo, R., El-Madany, T.S., Gonzalez-Cascon, R., Martín, M.P., Julitta, T., Moreno, G., Rascher, U., Reichstein, M., Rossini, M., Migliavacca, M., 2022. Heatwave breaks down the linearity between sun-induced fluorescence and gross primary production. New Phytol. 233, 2415–2428. https://doi.org/10.1111/nph.17920.
Meroni, M., Busetto, L., Colombo, R., Guanter, L., Moreno, J., Verhoef, W., 2010. Performance of spectral fitting methods for vegetation fluorescence quantification. Remote Sens. Environ. 114, 363–374. https://doi.org/10.1016/j.rse.2009.09.010.
Miao, G., Kaiyu, G., Xi, Y., Jin, W., Katherine, M., Yaping, C., Bin, P., Hyungsuk, K., 2018. Sun-induced chlorophyll fluorescence, photosynthesis, and light use efficiency of a soybean field from seasonally continuous measurements. J. Geophys. Res. Biogeosci. 123, 610–623. https://doi.org/10.1002/2017JG004180.
Mohammed, G.H., Colombo, R., Middleton, E.M., Rascher, U., van der Tol, C., Nedbal, L., Goulas, Y., Pérez-Priego, O., Damm, A., Meroni, M., Joiner, J., Cogliati, S., Verhoef, W., Malenovský, Z., Gastellu-Etchegorry, J.-P., Miller, J.R., Guanter, L., Moreno, J., Moya, I., Berry, J.A., Frankenberg, C., Zarco-Tejada, P.J., 2019. Remote sensing of solar-induced chlorophyll fluorescence (SIF) in vegetation: 50 years of progress. Remote Sens. Environ. 231, 111177 https://doi.org/10.1016/j.rse.2019.04.030.
Monneveux, P., Ramírez, D.A., Pino, M.-T., 2013. Drought tolerance in potato (S. Tuberosum L.): can we learn from drought tolerance research in cereals? Plant Sci. 205–206, 76–86. https://doi.org/10.1016/j.plantsci.2013.01.011.
Montero, D., Aybar, C., Mahecha, M.D., Martinuzzi, F., Söchting, M., Wieneke, S., 2023. A standardized catalogue of spectral indices to advance the use of remote sensing in earth system research. Sci Data 10, 197. https://doi.org/10.1038/s41597-023-02096-0.
Müller, P., Li, X.-P., Niyogi, K.K., 2001. Non-photochemical quenching. A response to excess light energy. Plant Physiol. 125, 1558–1566. https://doi.org/10.1104/pp.125.4.1558.
Pabon-Moreno, D.E., Migliavacca, M., Reichstein, M., Mahecha, M.D., 2022. On the potential of Sentinel-2 for estimating gross primary production. IEEE Trans. Geosci. Remote Sens. 60, 1–12. https://doi.org/10.1109/TGRS.2022.3152272.
Porcar-Castell, A., Tyystjärvi, E., Atherton, J., Tol, C., Flexas, J., Pfündel, E.E., Moreno, J., Frankenberg, C., Berry, J.A., 2014. Linking chlorophyll a fluorescence to photosynthesis for remote sensing applications: mechanisms and challenges. J. Exp. Bot. eru191 https://doi.org/10.1093/jxb/eru191.
Porcar-Castell, A., Malenovský, Z., Magney, T., Van Wittenberghe, S., Fernández-Marín, B., Maignan, F., Zhang, Y., Maseyk, K., Atherton, J., Albert, L.P., Robson, T. M., Zhao, F., Garcia-Plazaola, J.-I., Ensminger, I., Rajewicz, P.A., Grebe, S., Tikkanen, M., Kellner, J.R., Ihalainen, J.A., Rascher, U., Logan, B., 2021. Chlorophyll a fluorescence illuminates a path connecting plant molecular biology to earth-system science. Nat. Plants 7, 998–1009. https://doi.org/10.1038/s41477-021-00980-4.
Romero, J.M., Cordon, G.B., Lagorio, M.G., 2018. Modeling re-absorption of fluorescence from the leaf to the canopy level. Remote Sens. Environ. 204, 138–146. https://doi.org/10.1016/j.rse.2017.10.035.
Romero, J.M., Cordon, G.B., Lagorio, M.G., 2020. Re-absorption and scattering of chlorophyll fluorescence in canopies: a revised approach. Remote Sens. Environ. 246, 111860 https://doi.org/10.1016/j.rse.2020.111860.
Rossini, M., Nedbal, L., Guanter, L., Ač, A., Alonso, L., Burkart, A., Cogliati, S., Colombo, R., Damm, A., Drusch, M., Hanus, J., Janoutova, R., Julitta, T., Kokkalis, P., Moreno, J., Novotny, J., Panigada, C., Pinto, F., Schickling, A., Schüttemeyer, D., Zemek, F., Rascher, U., 2015. Red and far red Sun-induced chlorophyll fluorescence as a measure of plant photosynthesis. Geophys. Res. Lett. 42 https://doi.org/10.1002/2014GL062943, 2014GL062943.
Sadras, V.O., Milroy, S.P., 1996. Soil-water thresholds for the responses of leaf expansion and gas exchange: a review. Field Crop Res. 47, 253–266. https://doi.org/10.1016/0378-4290(96)00014-7.
Stuckens, J., Verstraeten, W.W., Delalieux, S., Swennen, R., Coppin, P., 2009. A dorsiventral leaf radiative transfer model: development, validation and improved model inversion techniques. Remote Sens. Environ. 113, 2560–2573. https://doi.org/10.1016/j.rse.2009.07.014.
Sun, Y., Frankenberg, C., Jung, M., Joiner, J., Guanter, L., Köhler, P., Magney, T., 2018. Overview of solar-induced chlorophyll fluorescence (SIF) from the orbiting carbon Observatory-2: retrieval, cross-mission comparison, and global monitoring for GPP. Remote Sens. Environ. 209, 808–823. https://doi.org/10.1016/j.rse.2018.02.016.
van der Tol, C., Verhoef, W., Timmermans, J., Verhoef, A., Su, Z., 2009. An integrated model of soil-canopy spectral radiances, photosynthesis, fluorescence, temperature and energy balance. Biogeosciences 6, 3109–3129. https://doi.org/10.5194/bg-6-3109-2009.
van der Tol, C., Berry, J.A., Campbell, P.K.E., Rascher, U., 2014. Models of fluorescence and photosynthesis for interpreting measurements of solar-induced chlorophyll fluorescence. J. Geophys. Res. Biogeosci. 119, 2312–2327. https://doi.org/10.1002/2014JG002713.
Van Wittenberghe, S., Alonso, L., Verrelst, J., Hermans, I., Delegido, J., Veroustraete, F., Valcke, R., Moreno, J., Samson, R., 2013. Upward and downward solar-induced chlorophyll fluorescence yield indices of four tree species as indicators of traffic pollution in Valencia. Environ. Pollut. 173, 29–37. https://doi.org/10.1016/j.envpol.2012.10.003.
Van Wittenberghe, S., Alonso, L., Verrelst, J., Moreno, J., Samson, R., 2015. Bidirectional sun-induced chlorophyll fluorescence emission is influenced by leaf structure and light scattering properties — a bottom-up approach. Remote Sens. Environ. 158, 169–179. https://doi.org/10.1016/j.rse.2014.11.012.
Van Wittenberghe, S., Alonso, L., Malenovský, Z., Moreno, J., 2019. In vivo photoprotection mechanisms observed from leaf spectral absorbance changes showing VIS–NIR slow-induced conformational pigment bed changes. Photosynth. Res. 142, 283–305. https://doi.org/10.1007/s11120-019-00664-3.
Van Wittenberghe, S., Sabater, N., Cendrero-Mateo, M.P., Tenjo, C., Moncholi, A., Alonso, L., Moreno, J., 2021. Towards the quantitative and physically-based interpretation of solar-induced vegetation fluorescence retrieved from global imaging. Photosynthetica 59, 438–457. https://doi.org/10.32615/ps.2021.034.
Vienne, A., Poblador, S., Portillo-Estrada, M., Hartmann, J., Ijiehon, S., Wade, P., Vicca, S., 2022. Enhanced weathering using basalt rock powder: carbon sequestration, co-benefits and risks in a mesocosm study with *Solanum tuberosum*. Front. Clim. 4.
Vilfan, N., van der Tol, C., Muller, O., Rascher, U., Verhoef, W., 2016. Fluspect-B: a model for leaf fluorescence, reflectance and transmittance spectra. Remote Sens. Environ. 186, 596–615. https://doi.org/10.1016/j.rse.2016.09.017.
Vilfan, N., Van der Tol, C., Yang, P., Wyber, R., Malenovský, Z., Robinson, S.A., Verhoef, W., 2018. Extending Fluspect to simulate xanthophyll driven leaf reflectance dynamics. Remote Sens. Environ. 211, 345–356. https://doi.org/10.1016/j.rse.2018.04.012.
Vilhar, U., 2016. Comparison of drought stress indices in beech forests: a modelling study. iForest - Biogeosci. For. 9, 635. https://doi.org/10.3832/ifor1630-008.
Viña, A., Gitelson, A.A., 2005. New developments in the remote estimation of the fraction of absorbed photosynthetically active radiation in crops. Geophys. Res. Lett. 32, L17403. https://doi.org/10.1029/2005GL023647.
Wang, Q., Moreno-Martínez, Á., Muñoz-Marí, J., Campos-Taberner, M., Camps-Valls, G., 2023a. Estimation of vegetation traits with kernel NDVI. ISPRS J. Photogramm. Remote Sens. 195, 408–417. https://doi.org/10.1016/j.isprsjprs.2022.12.019.
Wang, N., Yang, P., Clevers, J.G.P.W., Wieneke, S., Kooistra, L., 2023b. Decoupling physiological and non-physiological responses of sugar beet to water stress from sun-induced chlorophyll fluorescence. Remote Sens. Environ. 286, 113445 https://doi.org/10.1016/j.rse.2022.113445.
Wieneke, S., Burkart, A., Cendrero-Mateo, M.P., Julitta, T., Rossini, M., Schickling, A., Schmidt, M., Rascher, U., 2018. Linking photosynthesis and sun-induced fluorescence at sub-daily to seasonal scales. Remote Sens. Environ. 219, 247–258. https://doi.org/10.1016/j.rse.2018.10.019.
Wieneke, S., Balzarolo, M., Asard, H., Abd Elgawad, H., Peñuelas, J., Rascher, U., Ven, A., Verlinden, M.S., Janssens, I.A., Vicca, S., 2022. Fluorescence ratio and photochemical reflectance index as a proxy for photosynthetic quantum efficiency of photosystem II along a phosphorus gradient. Agric. For. Meteorol. 322, 109019 https://doi.org/10.1016/j.agrformet.2022.109019.
Wohlfahrt, G., Gerdel, K., Migliavacca, M., Rotenberg, E., Tatarinov, F., Müller, J., Hammerle, A., Julitta, T., Spielmann, F.M., Yakir, D., 2018. Sun-induced fluorescence and gross primary productivity during a heat wave. Sci. Rep. 8, 14169. https://doi.org/10.1038/s41598-018-32602-z.
Xu, S., Atherton, J., Riikonen, A., Zhang, C., Oivukkamäki, J., MacArthur, A., Honkavaara, E., Hakala, T., Koivumäki, N., Liu, Z., Porcar-Castell, A., 2021. Structural and photosynthetic dynamics mediate the response of SIF to water stress in a potato crop. Remote Sens. Environ. 263, 112555 https://doi.org/10.1016/j.rse.2021.112555.
Yang, K., Ryu, Y., Dechant, B., Berry, J.A., Hwang, Y., Jiang, C., Kang, M., Kim, J., Kimm, H., Kornfeld, A., Yang, X., 2018. Sun-induced chlorophyll fluorescence is more strongly related to absorbed light than to photosynthesis at half-hourly resolution in a rice paddy. Remote Sens. Environ. 216, 658–673. https://doi.org/10.1016/j.rse.2018.07.008.
Yang, P., van der Tol, C., Campbell, P.K.E., Middleton, E.M., 2020. Fluorescence correction vegetation index (FCVI): a physically based reflectance index to separate

physiological and non-physiological information in far-red sun-induced chlorophyll fluorescence. Remote Sens. Environ. 240, 111676 https://doi.org/10.1016/j.rse.2020.111676.

Yang, P., Prikaziuk, E., Verhoef, W., van der Tol, C., 2021. SCOPE 2.0: a model to simulate vegetated land surface fluxes and satellite signals. Geosci. Model Dev. 14, 4697–4712. https://doi.org/10.5194/gmd-14-4697-2021.

Yang, X., Li, R., Jablonski, A., Stovall, A., Kim, J., Yi, K., Ma, Y., Beverly, D., Phillips, R., Novick, K., Xu, X., Lerdau, M., 2023. Leaf angle as a leaf and canopy trait: rejuvenating its role in ecology with new technology. Ecol. Lett. 26, 1005–1020. https://doi.org/10.1111/ele.14215.

Zeng, Y., Badgley, G., Dechant, B., Ryu, Y., Chen, M., Berry, J.A., 2019. A practical approach for estimating the escape ratio of near-infrared solar-induced chlorophyll fluorescence. Remote Sens. Environ. 232, 111209 https://doi.org/10.1016/j.rse.2019.05.028.

Zeng, Y., Hao, D., Badgley, G., Damm, A., Rascher, U., Ryu, Y., Johnson, J., Krieger, V., Wu, S., Qiu, H., Liu, Y., Berry, J.A., Chen, M., 2021. Estimating near-infrared reflectance of vegetation from hyperspectral data. Remote Sens. Environ. 267, 112723 https://doi.org/10.1016/j.rse.2021.112723.

Zhang, Y., Guanter, L., Berry, J.A., van der Tol, C., Yang, X., Tang, J., Zhang, F., 2016. Model-based analysis of the relationship between sun-induced chlorophyll fluorescence and gross primary production for remote sensing applications. Remote Sens. Environ. 187, 145–155. https://doi.org/10.1016/j.rse.2016.10.016.

Zhao, F., Ma, W., Köhler, P., Ma, X., Sun, H., Verhoef, W., Zhao, J., Huang, Y., Li, Z., Ratul, A.K., 2022. Retrieval of red solar-induced chlorophyll fluorescence with TROPOMI on the Sentinel-5 precursor Mission. IEEE Trans. Geosci. Remote Sens. 60, 1–14. https://doi.org/10.1109/TGRS.2022.3162726.